

Electron-impact ionization of atomic hydrogenM. Baertschy,¹ T. N. Rescigno,^{2,3} W. A. Isaacs,² X. Li,² and C. W. McCurdy^{2,4}¹*Joint Institute for Laboratory Astrophysics, Boulder, Colorado 80309-0440*²*Computing Sciences Division, Lawrence Berkeley National Laboratory, Berkeley, California 94720*³*Physics Directorate, Lawrence Livermore National Laboratory, Livermore, California 94550*⁴*Department of Applied Science, University of California, Davis, Livermore, California 94550*

(Received 28 June 2000; published 18 January 2001)

Exterior complex scaling enables one to solve the time-independent Schrödinger equation for three charged particles without explicitly imposing the asymptotic boundary condition for three-body breakup. We have used this formalism to study electron-impact ionization of atomic hydrogen by directly solving for the radial components of the scattered wave on a complex, exterior scaled numerical grid. Computational procedures, presented briefly elsewhere [T. N. Rescigno, M. Baertschy, W. A. Isaacs, and C. W. McCurdy, *Science* **286**, 2474 (1999)], are discussed here in greater detail and additional results are presented. Our method is limited only by the finite size of the grid and the number of partial-wave components retained in the expansion of the wave function and, unlike other methods that have been used to study ionization, involves no uncontrolled approximations. Our calculated triply differential cross sections at 17.6, 20, 25, and 30 eV are found to be in excellent agreement with recent measurements.

DOI: 10.1103/PhysRevA.63.022712

PACS number(s): 34.80.Dp, 02.60.Dc, 02.70.Bf, 31.15.-p

I. INTRODUCTION

Electron-impact ionization of atomic hydrogen is the simplest example of an important class of problems in atomic collision theory that have persistently resisted numerical solution. The formal theory has been known for some time, beginning with the work of Peterkop [1] and of Rudge and Seaton [2] in the 1960s, who derived the form of the wave function for three charged particles in the “far” asymptotic region where all three particles are well separated, through the more recent work of Alt and Mukhamedzhanov [3], who derived a solution of the three-charged-particle Schrödinger equation which is valid in all asymptotic regions. Following the pioneering work of Brauner *et al.* [4], there have been many “ansatz” studies over the past decade in which aspects of the asymptotic wave function for three charged particles are incorporated into various types of distorted-wave formulas for the ionization amplitude, with varying degrees of success [5,6]. Much of this work is summarized in a recent review by Lucey, Rasch, and Whelan [7]. The formal theory, however, has not to date provided a viable path to an “exact” computational approach to the problem.

Two-body, close-coupling expansions are being applied to electron-atom scattering above the ionization threshold with renewed vigor, following the stunning demonstration of Bray and Stelbovics in 1993 [8] that such expansions can be made “convergent” for both excitation and total ionization cross sections. More recent attempts to extend these methods to the calculation of differential cross sections for electron-impact ionization have been only partially successful, yielding singly differential cross sections that oscillate about the correct values [9] and triple differential cross sections that display the correct relative angular behavior but require multiplication by unforeseeable constants [10,11] to be compatible with experiment. The magnitude of these effects diminishes with increasing collision energy as the ionization cross sections become better described by perturbation theory. Re-

cent work [12] has shown that such spurious behavior is not necessarily connected to the long-range Coulomb interactions between charged particles, but rather is connected to the methods used to extract information about three-body breakup from a wave function that is matched to a sum of discretized two-body channels.

In several previous papers [13,14], we outlined a strategy for computing ionization cross sections by a route that completely avoids explicit specification of asymptotic boundary conditions. We use exterior complex scaling [15] of all interparticle distances to simplify the asymptotic boundary conditions for scattering. With this mathematical transformation of the Schrödinger equation we can calculate the scattered wave portion of the full wave function to arbitrary accuracy on a finite region of space. Scattering information is extracted by applying the quantum-mechanical flux operator to the computed wave function at several finite distances and numerically extrapolating to infinite distances in order to obtain differential cross sections for ionization.

Previously, we demonstrated the viability of this procedure with calculations of total and differential ionization cross sections for atomic hydrogen in the *s*-wave (Temkin-Poet) model of e^- -H scattering [16]. The Temkin-Poet model [17,18] keeps only states of zero angular momentum for each electron, leaving a simplified, two-dimensional problem, but one with the same pathologies in the asymptotic boundary conditions as the full problem. We have since extended the method to a treatment of the full electron-hydrogen ionization problem and recently announced the results of this treatment [19], including triply differential cross sections at one energy (17.6 eV) for which absolute measurements are available for comparison. In this paper we give a detailed description of the computational procedures that were employed and report results at several other energies.

Exterior complex scaling may solve the problem of intractable scattering boundary conditions, but calculating the scat-

tered wave on a large enough region to obtain accurate ionization information still poses an enormous computational challenge. We calculate the radial functions in a partial wave expansion of the scattered wave function directly onto a large, two-dimensional grid. The coupled, two-dimensional differential equations that must be solved to obtain the radial functions lead to systems of as many as five million complex, linear equations for the calculations reported here. We solved these coupled equations using a distributed memory, parallel supercomputer to implement an iterative algorithm with preconditioners specifically tailored to the problem at hand.

Technical reasons connected with the use of complex scaling require us to truncate the interaction potentials on the complex portions of the grid [20]. The physically correct results are then recovered by extrapolating the computed values to infinite box size. Because we cannot offer a strict mathematical proof that this extrapolation yields the exact value, we have carried out a number of numerical tests to show that the procedures employed are in fact producing the correct result. For instance, we will show that the radial wave functions we obtain by exterior complex scaling display the three-body logarithmic phase distortion that must characterize an exact solution. In the course of our previous work with the Temkin-Poet model, we studied the effects of finite box size on the accuracy of the extrapolated results and found that within certain limitations the results are, indeed, correct. The fact that there have been new results [21] reported recently on ionization cross sections in the Temkin-Poet model, which were obtained by a completely different method, that agree with our previously published results, gives us added confidence in the soundness of our method. Ultimately, however, the fundamental correctness of our procedure relies on the empirical observation that the computed results are in perfect agreement with absolute experimental measurements that probe the most intimate details of the collision dynamics at energies where long-range correlation effects are very important.

Our method consists of two steps: (i) computing the scattered wave part of the total wave function without explicit reference to any asymptotic form and (ii) extracting detailed information for electron-impact ionization from the computed wave function, again without explicit reference to an asymptotic form. We describe our method for calculating the scattered wave in Secs. II A and II B. Simplification of the scattering boundary conditions with exterior complex scaling is outlined in the latter section. In Sec. III we describe details of the numerical and computational methods we used to solve the Schrödinger equation on a complex grid. In Sec. IV we describe properties of the scattered wave through examination of its radial components and give a number of illustrative examples. In Sec. V we describe the numerical procedures we used to extract dynamical information from the computed wave functions and to compute differential cross sections. Our results for singly and triply differential cross sections are presented in Sec. VI. Section VII contains concluding remarks.

II. THEORETICAL APPROACH

A. Scattered-wave formalism

Our approach to the electron-impact ionization problem was outlined in two previous papers [13,14]. The method consists of two distinct steps. The first entails a calculation of the outgoing wave portions of the wave function without recourse to any explicit asymptotic form. This is accomplished by applying an exterior complex scaling transformation to the radial electron coordinates. The second step requires a procedure for extracting dynamical information from the scattered waves, again without explicit reference to an asymptotic form. To accomplish the extraction, we apply quantum-mechanical flux operators to the computed wave functions.

We begin by partitioning the total wave function into an appropriately symmetrized unperturbed state $\Psi_{k_i}^0$, describing a free electron incident with momentum \mathbf{k}_i on a ground-state hydrogen atom

$$\Psi_{k_i}^0(\mathbf{r}_1, \mathbf{r}_2) = \frac{1}{\sqrt{2}} [\Phi_{1s}(\mathbf{r}_1) e^{i\mathbf{k}_i \cdot \mathbf{r}_2} + (-1)^s \Phi_{1s}(\mathbf{r}_2) e^{i\mathbf{k}_i \cdot \mathbf{r}_1}] \quad (1)$$

and a scattered wave term Ψ_{sc}^+ . The symmetry of the total wave function is determined by the magnitude of the total spin: it is either symmetric for total spin $S=0$ or antisymmetric for $S=1$. The scattered wave function Ψ_{sc}^+ is defined as

$$\Psi_{sc}^+(\mathbf{r}_1, \mathbf{r}_2) = G^+(E)(\hat{H} - E)\Psi_{k_i}^0(\mathbf{r}_1, \mathbf{r}_2), \quad (2)$$

or, equivalently, by a purely outgoing solution of the inhomogeneous differential equation

$$(E - \hat{H})\Psi_{sc}^+(\mathbf{r}_1, \mathbf{r}_2) = (\hat{H} - E)\Psi_{k_i}^0(\mathbf{r}_1, \mathbf{r}_2), \quad (3)$$

that comes from rearrangement of the Schrödinger equation with Hamiltonian \hat{H} ,

$$\hat{H}(\mathbf{r}_1, \mathbf{r}_2) = -\frac{1}{2}\nabla_1^2 - \frac{1}{2}\nabla_2^2 - \frac{1}{r_1} - \frac{1}{r_2} + \frac{1}{|\mathbf{r}_1 - \mathbf{r}_2|}. \quad (4)$$

Asymptotically, Ψ_{sc}^+ decomposes into a sum of discrete (elastic and excitation) two-body channels and a term Ψ_{ion}^+ that describes the ionization continuum

$$\Psi_{sc}^+(\mathbf{r}_1, \mathbf{r}_2) \sim \sum_{r_1, r_2 \rightarrow \infty} \sum_{n,l,m} \frac{1}{\sqrt{2}} \left[\Phi_{nlm}(\mathbf{r}_1) \frac{f_{nlm}(\hat{r}_2)}{r_2} e^{i\mathbf{k}_n \cdot \mathbf{r}_2} + (-1)^s (1 \leftrightarrow 2) \right] + \Psi_{ion}^+(\mathbf{r}_1, \mathbf{r}_2). \quad (5)$$

The discrete channel components factor into products of bound atomic states and one-electron continuum functions while the ionization term is intrinsically nonseparable [12]. In the far asymptotic region where all interparticle distances are large, the ionization term behaves as [22]

$$\Psi_{\text{ion}}^+(\mathbf{r}_1, \mathbf{r}_2) \underset{\rho \rightarrow \infty}{\sim} -f_i(\hat{r}_1, \hat{r}_2, \alpha) \sqrt{\frac{i\kappa^3}{\rho^5}} \times \exp\left\{i\left[\kappa\rho + \frac{\zeta(\hat{r}_1, \hat{r}_2, \alpha)}{\kappa} \ln(2\kappa\rho)\right]\right\}, \quad (6)$$

where f_i is the ionization amplitude and the hyperspherical coordinates are defined by $\rho = (r_1^2 + r_2^2)^{1/2}$ and $\alpha = \tan^{-1}(r_1/r_2)$ and κ is related to the total energy by $E = \kappa^2/2$. Note that the coefficient $\zeta(\hat{r}_1, \hat{r}_2, \alpha)$ depends on the energies and ejection angles of both electrons. Equation (6) is written only for illustrative purposes and is not explicitly part of our computational procedures.

Adopting a conventional partial-wave description, we expand both $\Psi_{k_i}^0$ and Ψ_{sc}^+ in coupled spherical harmonics

$$\mathcal{Y}_{l_1, l_2}^{LM}(\hat{r}_1, \hat{r}_2) = \sum_{m_1, m_2} \langle l_1 l_2 m_1 m_2 | LM \rangle Y_{l_1 m_1}(\hat{r}_1) Y_{l_2 m_2}(\hat{r}_2) \quad (7)$$

which are eigenfunctions of total angular momentum L and its projection M along the z axis (defined to be in the direction of \mathbf{k}_i). In Eq. (7) $l_1 m_1$ and $l_2 m_2$ refer to the orbital angular momenta of the individual electrons and $\langle l_1 l_2 m_1 m_2 | LM \rangle$ is a Clebsch-Gordan coefficient. For electrons incident on hydrogen in an initial s state, we need only the terms for which $M = 0$ in the expansions of $\Psi_{k_i}^0$ and Ψ_{sc}^+ ,

$$\Psi_{k_i}^0(\mathbf{r}_1, \mathbf{r}_2) = \sum_{L=0}^{\infty} \frac{i^L \sqrt{2\pi(2L+1)}}{r_1 r_2 k_i} \times [\phi_{nl}(r_1) \hat{j}_L(k_i r_2) \mathcal{Y}_{0,L}^{L0}(\hat{r}_1, \hat{r}_2) + (-1)^s \hat{j}_L(k_i r_1) \phi_{nl}(r_2) \mathcal{Y}_{L,0}^{L0}(\hat{r}_1, \hat{r}_2)], \quad (8)$$

$$\Psi_{\text{sc}}^+(\mathbf{r}_1, \mathbf{r}_2) = \frac{1}{r_1 r_2} \sum_{L, l_1, l_2} \psi_{l_1 l_2}^L(r_1, r_2) \mathcal{Y}_{l_1, l_2}^{L0}(\hat{r}_1, \hat{r}_2). \quad (9)$$

Since both total angular momentum and parity [23] are conserved quantities, the sums can be limited to terms for which $L + l_1 + l_2$ is even.

Substitution of the angular expansions defined in Eqs. (8) and (9) into the scattered wave equation, Eq. (3), gives a set of coupled, two-dimensional equations for the radial functions $\psi_{l_1 l_2}^L$ for each value of L and S ,

$$[E - \hat{H}_{l_1}(r_1) - \hat{H}_{l_2}(r_2)] \psi_{l_1 l_2}^L(r_1, r_2) - \sum_{l'_1, l'_2} \langle l_1 l_2 || l'_1 l'_2 \rangle_L \psi_{l'_1 l'_2}^L(r_1, r_2) = \chi_{l_1 l_2}^L(r_1, r_2). \quad (10)$$

In Eq. (10), $\hat{H}_l(r)$ is the radial hydrogenic Hamiltonian,

$$\hat{H}_l(r) \equiv -\frac{1}{2} \frac{d^2}{dr^2} + \frac{l(l+1)}{2r^2} - \frac{1}{r} \quad (11)$$

and the radial coupling potentials $\langle l_1 l_2 || l'_1 l'_2 \rangle_L$ are obtained by taking matrix elements of $1/|\mathbf{r}_1 - \mathbf{r}_2|$ between two coupled spherical harmonics

$$\langle l_1 l_2 || l'_1 l'_2 \rangle_L \equiv \langle l_1 l_2 L 0 | \frac{1}{|\mathbf{r}_1 - \mathbf{r}_2|} | l'_1 l'_2 L 0 \rangle = \sum_{\lambda} C_{l_1 l_2 l'_1 l'_2}^{L, \lambda} \frac{r_{<}^{\lambda}}{r_{>}^{\lambda+1}}, \quad (12)$$

where $r_{<} (r_{>})$ is the lesser (greater) of r_1 and r_2 and Dirac notation denotes integration over the angular coordinates of both electrons. The coefficients $C_{l_1 l_2 l'_1 l'_2}^{L, \lambda}$ are discussed by Percival and Seaton [23]. The inhomogeneous term $\chi_{l_1 l_2}^L$ that appears on the right-hand side of Eq. (10) arises from the partial-wave expansion of $(\hat{H} - E)\Psi_{k_i}^0$,

$$\chi_{l_1 l_2}^L = \frac{i^L}{k_i} \sqrt{2\pi(2L+1)} \times \left[\langle l_1 l_2 || 0L \rangle_L - \frac{1}{r_2} \delta_{l_1 0} \delta_{l_2 L} \right] \times [\phi_{nl}(r_1) \hat{j}_L(k_i r_2) + (-1)^s (1 \leftrightarrow 2)]. \quad (13)$$

In a conventional approach, one would attempt to solve the coupled equations represented in Eq. (10) by applying the correct scattering boundary conditions [Eq. (5)] to each of the $\psi_{l_1 l_2}^L$. The fact that such a task has, to date, never been carried out testifies to the intractability of such an approach. Without a viable means for explicitly imposing the correct asymptotic boundary conditions for the ionization components of the $\psi_{l_1 l_2}^L$, we need an alternative approach, one that addresses the outgoing wave character of the scattered wave without explicitly imposing detailed asymptotic boundary conditions. Exterior complex scaling of the radial coordinates provides such a path, simplifying the outgoing wave boundary conditions and allowing the $\psi_{l_1 l_2}^L$ to be calculated correctly over a finite region of space.

B. Exterior complex scaling

The method of complex rotation or complex scaling, in which all interparticle coordinates are rotated by a fixed angle into the complex plane, is well known in physics, both as a formal mathematical device in nonrelativistic scattering theory and as a powerful computational tool [24]. Most applications of complex scaling in atomic and molecular physics have centered on the calculation of resonance energies and lifetimes, which are related to the discrete eigenvalues of the Hamiltonian under complex rotation. An important early extension of complex scaling was Simon's exterior complex scaling procedure (ECS) [15], in which coordinates are only scaled outside a (hyper)sphere of radius R_0 . This extension was motivated by the desire to treat Hamiltonian interactions

that may have interior nonanalyticities, such as the Born-Oppenheimer Hamiltonian viewed solely as a function of electronic coordinates [25], or that are only known numerically on a finite region of coordinate space. The ECS procedure has made it possible to carry out direct resonance calculations on a variety of molecular problems.

Complex scaling techniques can also be used, with certain caveats, to calculate scattering cross sections without explicitly enforcing asymptotic boundary conditions. Apart from applications to photoionization [26,27], this area has received far less attention than complex scaling in connection with resonances. A solution of the full scattering problem requires matrix elements of the resolvent between functions of the form $V(r)\sin(kr)$ and these diverge under complex rotation unless the interaction potential, $V(r)$, is exponentially bounded [28]. This fact had, until recently [20], posed a major obstacle to using complex scaling to solve scattering problems with long-range interactions. The key to applying the ECS procedure to long-range potential problems is to truncate the interaction potential at the boundary of the hypersphere and to either carry out calculations with R_0 large enough that the truncation of the potential is of no physical consequence or, if this is impractical, to carry out calculations for different values of R_0 and perform a numerical extrapolation of $R_0 \rightarrow \infty$ to obtain the physically correct results.

We take the ECS transformation as a mapping, $r \rightarrow z(r)$, of all radial coordinates to a contour

$$z(r) \equiv \begin{cases} r, & r < R_0 \\ R_0 + (r - R_0)e^{i\eta}, & r \geq R_0 \end{cases} \quad (14)$$

that is real for $r < R_0$, but rotated into the upper half of the complex plane beyond R_0 . In two dimensions the contour defined in Eq. (14) defines an interior box of length R_0 (see Fig. 1) in which both radial coordinates are real. Outside of that box one or both coordinates are complex.

The transformation has the desirable property that any outgoing wave evaluated on the contour Eq. (14) dies exponentially as the coordinates get large. Thus, the ECS procedure transforms any outgoing wave into a function that falls off exponentially outside R_0 but is equal to the infinite range wave over the finite region of space where the coordinates are real. If we apply this transformation to both radial coordinates in the coupled equations [Eq. (10)] and require the solutions to vanish for values of the radial coordinates well beyond R_0 (in practice, we discretize the coordinates onto a finite grid and require the solutions to vanish at the grid boundaries), we will obtain complex-scaled $\psi_{l_1 l_2}^L$ that are exponentially decaying functions outside of the interior region shown in Fig. 1. The fact that these are the physical solutions we seek can be seen as follows. A general solution of the inhomogeneous scattered wave equation [Eq. (3)] can be written as a linear combination of the particular solution defined by Eq. (2), which is purely outgoing, plus any solution of the corresponding homogeneous equation. Solutions of the latter, however, which are regular at the origin, would contain plane-wave terms that diverge under complex scaling

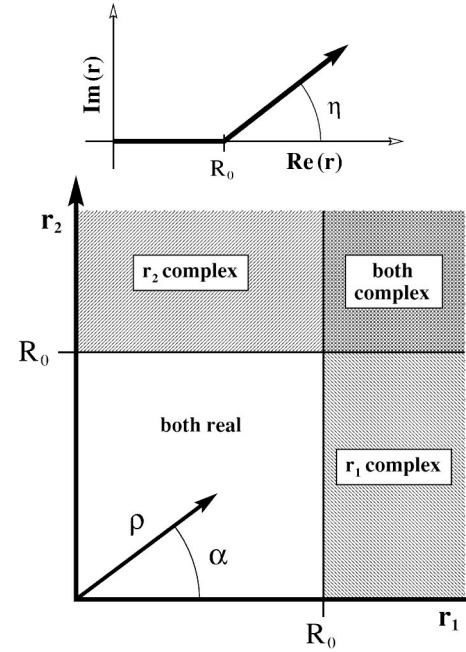


FIG. 1. On the top is an illustration of the ECS contour rotated into the upper half of the complex r plane beyond R_0 . On the bottom is a depiction of exterior complex scaling for two radial coordinates.

and are thus excluded from any numerical solution by our choice of boundary conditions.

The coupled equations [Eq. (10)] are transformed by evaluating the derivatives, all potentials, and the inhomogeneous terms $\chi_{l_1 l_2}^L$ on the complex contours. This requires some care to ensure the derivatives are taken along the complex contour, particularly at the point $r = R_0$ where the contour has a discontinuous first derivative. Transforming the one-electron potentials is simply a matter of evaluating the Coulomb potentials for complex values. We handle the two-electron potentials by applying the ECS transformation separately to the regions $r_1 < r_2$ and $r_1 > r_2$. As previously stated, we cannot apply the ECS transformation to the inhomogeneous terms on the right-hand side of Eq. (10) because the potential terms do not fall off rapidly enough to overcome the exponential increase of the free functions along the complex part of the contour, making it necessary to truncate the long-range Coulomb potentials at R_0 in the inhomogeneous terms $\chi_{l_1 l_2}^L$ [20]. This is the only source of systematic error in our scheme for calculating the scattered wave with exterior complex scaling. The numerical procedures we employed to minimize this source of error will be addressed below.

Solving the coupled equations transformed in this way gives the $\psi_{l_1 l_2}^L$ evaluated along the complex contours. In practice, it is simpler to think of the $\psi_{l_1 l_2}^L$ calculated under ECS as functions of the real coordinates r_1 and r_2 . Thus, we treat the calculated $\psi_{l_1 l_2}^L$ as nonanalytic functions of r_1 and r_2 (with an enforced discontinuity of the first derivatives with respect to the radial coordinates at the turning point) rather than as analytic functions evaluated along the contour. For the remainder of this paper we shall use $\psi_{l_1 l_2}^L(r_1, r_2)$ to

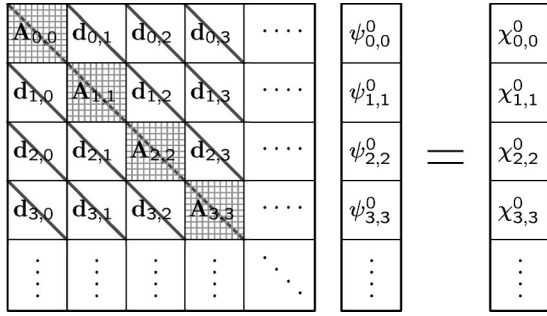


FIG. 2. Block matrix structure of the coupled equations using $L=0$ as an example.

refer to the complex-scaled radial functions. In the region $r_1, r_2 < R_0$ the calculated $\psi_{l_1 l_2}^L$ are the same as the unscaled $\psi_{l_1 l_2}^L$ aside from the effects of contributions from high- n bound states of hydrogen caused by truncating the Coulomb potentials in the $\chi_{l_1 l_2}^L$.

III. COMPUTATIONAL PROCEDURES

A. High-order finite difference methods

We solve for the $\psi_{l_1 l_2}^L$ directly on a two-dimensional radial grid using finite difference approximations for the derivatives. The coupled equations are represented by a matrix with the block structure illustrated in Fig. 2 where the dimension of each block is the total number of two-dimensional (2D) grid points, which we denote as N , and the number of blocks is the number of partial wave channels retained in the coupled equations. Diagonal blocks, $\mathbf{A}_{l_1 l_2}$,

$$\mathbf{A}_{l_1, l_2} \equiv E - \hat{H}_{l_1}(r_1) - \hat{H}_{l_2}(r_2) - \langle l_1 l_2 \| l_1, l_2 \rangle_L \quad (15)$$

are matrix representations of two-dimensional, uncoupled radial equations while the off-diagonal blocks are the coupling potentials $\langle l_1 l_2 \| l'_1 l'_2 \rangle_L$ with $(l'_1, l'_2) \neq (l_1, l_2)$.

Producing meaningful ionization information at energies several eV above the ionization threshold requires knowing Ψ_{sc}^+ at a distance of at least $100a_0$. The grid must extend beyond R_0 far enough to allow the complex-scaled radial functions to decay effectively to zero at the edge of the grid. We used grids that extend an additional $25a_0$ beyond R_0 .

With seven-point finite difference approximations to the second derivatives (accurate to sixth-order in the grid spacing), four grid points per a_0 are sufficient to represent oscillatory functions with energies ≤ 40 eV. However, a more densely spaced grid is needed to represent the Coulomb potential at small distances. We used a spacing of $0.25a_0$ over most of the grid with a spacing of $0.05a_0$ for r_1 and r_2 values less than $2.0a_0$. Beyond R_0 it is possible to use larger grid spacings without affecting the accuracy of the wave function where the coordinates are real.

Finite difference formulas that sample regions of two different grid spacings are less accurate by one order of magnitude than their uniformly spaced grid counterparts. We used specialized seven-point finite difference formulas (ac-

curate to fifth order) to span the interfaces between regions of different grid spacings. An advantage of using higher-order finite difference is that it allows the grid to be partitioned into regions of different grid spacing without a significant increase in numerical error. Further details about the high-order finite difference along with the explicit formulas we used are given in the Appendix.

Complex-scaled radial functions $\psi_{l_1 l_2}^L(z(r_1), z(r_2))$ evaluated on the contour defined in Eq. (14) are continuous functions of r_1 and r_2 whose first derivatives are discontinuous across R_0 . Finite difference is one of the few numerical methods that can be made compatible with this contour [20]. Formulas for the derivatives are generalized to ECS by multiplying grid spacings by $e^{i\eta}$ beyond R_0 . This produces exactly the required nonanalyticity in the calculated $\psi_{l_1 l_2}^L$ provided that R_0 is one of the grid points [29]. The specialized finite difference formulas we used to span the interface between regions of different grid spacing must also be used to span R_0 , even for uniformly spaced grids.

B. Numerical methods for large, sparse linear systems

A typical radial grid with $R_0 = 110a_0$ consists of 498 grid points in one dimension with each $\psi_{l_1 l_2}^L$ represented by 248004 values. Keeping 16 partial wave channels in the coupled equations for a particular L leads to a linear system on the order of four million. Solving a linear system of this size by Gaussian elimination is impractical, so we must use an iterative algorithm to solve the coupled equations. The eigenvalue spectrum of a complex-scaled Hamiltonian is such that no known iterative algorithm will converge to solution without preconditioning. Therefore, finding a suitable preconditioner for the coupled equations is a necessity. A preconditioner should be a simplified linear system that has an eigenvalue spectrum similar to the original system. The set of *uncoupled* radial equations, defined by setting $\langle l_1 l_2 \| l'_1 l'_2 \rangle_L = 0$ for all $(l'_1, l'_2) \neq (l_1, l_2)$ in Eq. (10), have numerical properties similar to the coupled equations, but require solving linear systems only as big as the total number of radial grid points. We have found solutions of the uncoupled equations to be a suitable preconditioner for solving the coupled equations. Previously, we treated the Temkin-Poet model problem [17,18] (equivalent to the $L=l_1=l_2=0$ uncoupled radial equation) on very large radial grids [16]. Using the uncoupled equations as a pre-conditioner means solving several independent problems similar to the Temkin-Poet model, and we repeatedly employ the same numerical methods we used for the Temkin-Poet model to accomplish the preconditioning step. Convergence of the conjugate gradient squared (CGS) iterative algorithm [30], using solutions to the uncoupled equations as a block-diagonal preconditioner, is shown in Fig. 3 for several different values of L . Each CGS iteration required two solutions of the uncoupled equations, but with different right-hand sides.

The block matrix structure (see Fig. 2) of the coupled equations suggests a natural level of parallelism for the iterative algorithm that make it well suited for distributed memory, parallel computers. Each partial wave channel is

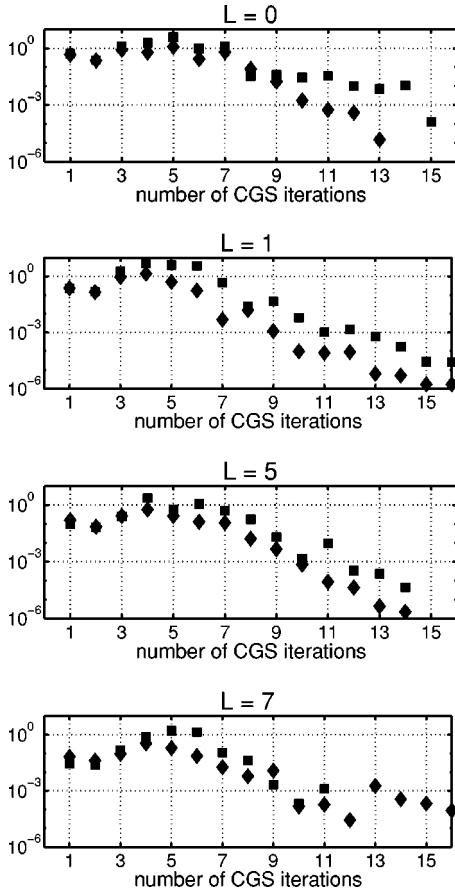


FIG. 3. Convergence of the CGS algorithm for the coupled equations with singlet spin symmetry for various total angular momenta L . Error in the calculated scattered wave is plotted for incident energies of 17.6 eV (squares) and 25 eV (diamonds).

assigned an independent group of processors. Solving the uncoupled equations, which is the most computationally intensive part of the iterative algorithm, is local to each group of processors. Matrix-vector products for the coupled equations involve calculating matrix-vector products for each diagonal block, which is local to each processor group, and for every off-diagonal block, which requires communication between different processor groups. The off-diagonal blocks, which are merely the coupling potentials evaluated on the

grid, are themselves diagonal matrices so adding each coupling term is a relatively inexpensive operation. Therefore, the bulk of the computations are local to each processor group.

A single uncoupled, two-dimensional, radial equation presents a linear system of $\sim 250\,000$ equations. In a recent study [16] using the Temkin-Poet model to test our formalism we solved linear systems of this type that were as large as 750 000. Even the uncoupled equations present very large linear systems and we found that iterative methods fail to converge if we used standard preconditioning techniques but could be made to work if we start with a trial solution that is a reasonable approximation to the true solution. To produce such a trial vector, we need a direct method of solution that exploits the structure of the linear equations.

Gaussian elimination (LU factorization), followed by forward and back substitutions (triangular solutions), is a classic method of solving a linear system $AX=b$. One key advantage of this “direct” method over the iterative methods is its *robustness*, in the sense that it involves a fixed number of floating-point operations (dependent only on the matrix dimension) even if the linear system is ill conditioned. For example, for a dense matrix of size $N \times N$, LU factorization requires $\frac{2}{3}N^3$ operations, and the subsequent solution step requires $2N^2$ operations. An advantage of using the finite difference is that the resulting matrices are very sparse and the LU factorizations can be carried out in far fewer operations than would be possible with dense matrices. The uncoupled radial equations have the structure of a two-dimensional, finite difference Laplacian matrix. With m -point finite difference formulas these matrices have, at most, $2m-1$ nonzero elements per row and the total number of nonzeros scales linearly with the number of grid points.

Since m -point finite difference applied to the uncoupled radial equations produces matrices that have only $O(N)$ nonzeros on $2m-1$ diagonals, as opposed to N^2 nonzeros in the dense case, significant savings in both time and memory can be achieved if we can exploit the sparsity structure of the matrix. One way to exploit sparsity is to use a *band* solver, such as that implemented in LAPACK [31], a widely used linear algebra package. Our matrix has bandwidth \sqrt{N} around the main diagonal. The band solver does not perform operations on the zeros outside the band, but it fills the non-

TABLE I. The order in which partial wave channels were chosen for each value of L in convergence studies.

$L=0$	(0,0), (1,1), (2,2), (3,3), (4,4), (5,5)
$L=1$	(0,1), (1,2), (2,3), (3,4), (4,5), (5,6)
$L=2$	(1,1), (0,2), (2,2), (1,3), (3,3), (2,4), (4,4), (3,5), (5,5), (4,6)
$L=3$	(1,2), (0,3), (2,3), (1,4), (3,4), (2,5), (4,5), (3,6), (5,6), (4,7)
$L=4$	(2,2), (1,3), (3,3), (0,4), (2,4), (4,4), (1,5), (3,5), (5,5), (2,6), (4,6), (6,6), (3,7), (7,7), (4,8)
$L=5$	(2,3), (1,4), (3,4), (0,5), (2,5), (4,5), (1,6), (3,6), (5,6), (2,7), (4,7), (6,7), (3,8), (5,8), (7,8), (4,9)
$L=6$	(0,6), (1,5), (2,4), (3,3), (1,7), (2,6), (3,5), (4,4), (2,8), (3,7), (4,6), (5,5), (3,9), (4,8)
$L=7$	(0,7), (1,6), (2,5), (3,4), (1,8), (2,7), (3,6), (4,5), (2,9), (3,8), (4,7), (5,6), (3,10)
$L=8$	(0,8), (1,7), (2,6), (3,5), (4,4), (1,9), (2,8), (3,7), (4,6), (5,5)
$L=9$	(0,9), (1,8), (2,7), (3,6), (4,5), (1,10), (2,9), (3,8), (4,7), (5,6)

zeros completely within the band in the L and U factor matrices. For the LU factorization, the number of operations is $O(N^2)$ and the number of nonzeros to be stored is $O(N^{3/2})$.

We can achieve even greater computational savings by employing a more general sparse solver, which does not rely on the band structure and allows for arbitrary patterns of sparseness. For example, if the equations and variables are reordered using *nested dissection* [32], the number of operations and the number of nonzeros are reduced to $O(N^{3/2})$ and $O(N \log N)$. Sparse solvers are thus asymptotically superior to band solvers, but, in practice, are much more difficult to develop. There are issues concerned with storing the nonzero matrix elements so that one column (or row) of the matrix can be rapidly extracted during the computation [30]. Second, and more problematic, there are usually more nonzeros in the L and U factors than in the original matrix A . These new nonzeros are called fills. (This is not an issue with iterative solvers where the matrix A is used only in matrix-vector multiplication and is not modified.) The amount of fill is influenced by the order of the equations and variables and there has been a considerable research effort in developing good ordering algorithms to minimize the fill [32,33]. There are also issues associated with designing efficient algorithms to detect the positions of the fills and set up the sparse matrix storage for L and U [34]. This involves manipulating a sequence of elimination graphs associated with each Gaussian elimination step. The calculations reported here were carried out with a state-of-the-art sparse solver called SUPERLU [35], which has been optimized to run on both sequential and parallel computer platforms. Sequential SUPERLU offers great performance compared to band solvers, but was incapable of solving the largest systems we considered with N on the order of hundreds of thousands or millions. The parallel version of SUPERLU we used was designed to enhance scalability and minimize interprocessor communication and load imbalance by using a two-dimensional block cyclic partitioning scheme to partition the L and U matrices on multiple processors [36].

With a linear solver that takes advantage of the sparsity of the matrix, there is considerable savings in computer time and memory that comes from using lower-order finite difference formulas. The strategy that ultimately proved successful for our problem was to carry out a direct solve, using SUPERLU, of the linear systems produced by a three-point finite difference approximation to the uncoupled equations. These low-order results had unacceptable numerical errors, but they did provide a good preconditioner for the iterative solution of linear systems based on a higher-order finite difference. We then solved the uncoupled, two-dimensional radial equations based on a seven-point finite difference with the CGS iterative algorithm using the three-point finite difference matrices as the preconditioner. As an example, direct (by LU factorization) solution of an uncoupled radial equation approximated by a seven-point finite difference on 114244 grid points took 1477 s using a 332 Mhz Power2 CPU. The CGS algorithm using the lowest-order finite difference matrix as a preconditioner converged in seven iterations and took only 464 s. Finally, the fully coupled set of linear equations was iteratively solved using the uncoupled

solutions as a preconditioner. Thus, the complete solution of the coupled equations used the CGS algorithm at two levels, first in solving the uncoupled equations with different order finite difference schemes and then again in an iterative solution of the coupled equations.

IV. PROPERTIES OF THE SCATTERED WAVE

The radial functions can be classified into three groups according to their symmetry properties. Singlet radial func-

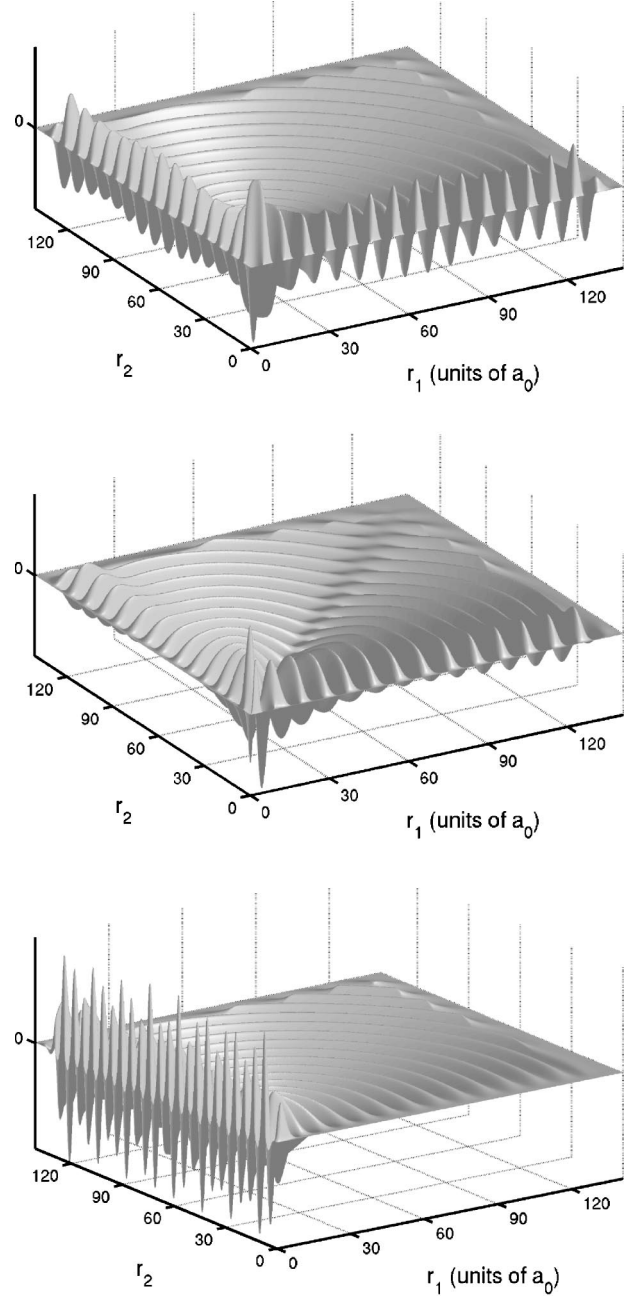


FIG. 4. Real parts of three representative radial functions for electron-hydrogen scattering at 17.6-eV incident energy. The upper picture shows the singlet, $L=2$ and $l_1=l_2=1$ radial function. The middle picture shows the triplet, $L=2$ and $l_1=l_2=2$ radial function. The lower picture shows the singlet, $L=3$, $l_1=0$, and $l_2=3$ radial function.

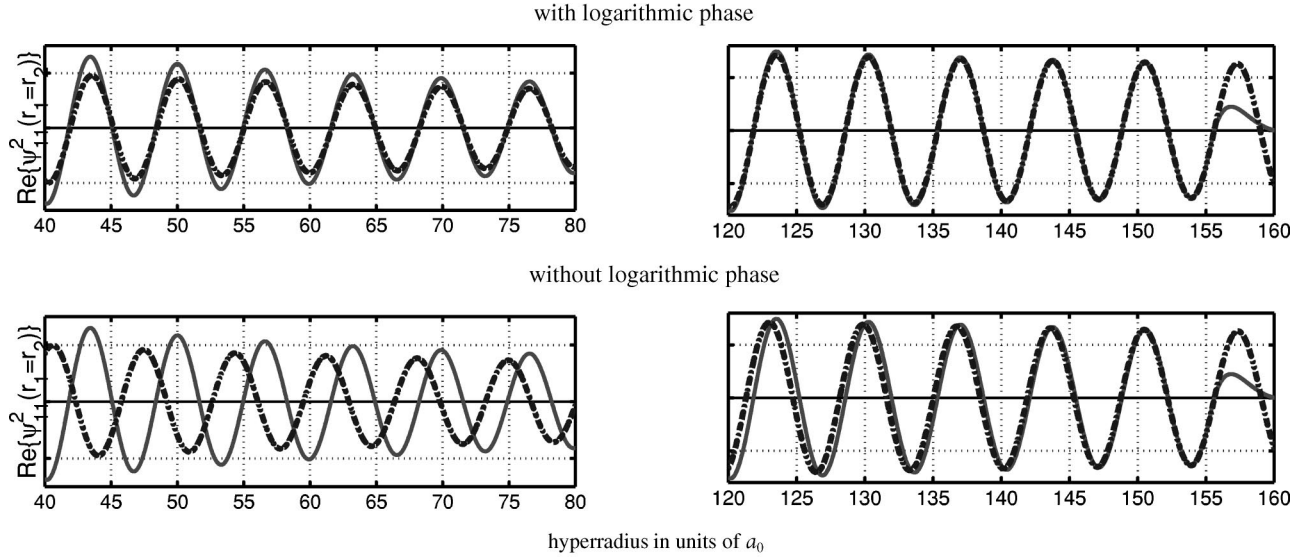


FIG. 5. Calculated $\psi_{l_1 l_2}^L$ (solid line) at an incident energy of 30 eV for $L=2$ and $l_1=l_2=1$ compared, along $r_1=r_2$, to $(A/\sqrt{\rho})e^{i[\kappa\rho+B\ln(\kappa\rho)+\delta]}$ (dashed line). In the upper panels A , B , and δ were chosen to best fit the radial function at large distances. At smaller distances this same choice of parameters still gives a good fit to the phase. In the lower panels a similar functional fit was attempted without a logarithmic phase (i.e., setting $B=0$). This functional form is able to match in phase only over short distances.

tions with $l_1=l_2$ are symmetric about $r_1=r_2$ while their triplet counterparts are antisymmetric. All radial functions with $l_1\neq l_2$ are asymmetric. These symmetry properties can be summed up with the relation

$$\psi_{l_2 l_1}^L(r_2, r_1) = (-1)^s \psi_{l_1 l_2}^L(r_1, r_2) \quad (16)$$

which follows directly from the required symmetry of the partial wave expansion in Eq. (9). Note that for every $\psi_{l_1 l_2}^L(r_1, r_2)$ with $l_1\neq l_2$ that is included in the expansion we must also be sure to include its counterpart $\psi_{l_2 l_1}^L(r_1, r_2)$ in order to maintain the symmetry of the overall scattered wave. In our calculations we take advantage of the symmetry properties of the radial functions by explicitly storing only those $\psi_{l_1 l_2}^L$ for which $l_1\leq l_2$. The $\psi_{l_1 l_2}^L$ with $l_2>l_1$ are then included implicitly, using the relation in Eq. (16), when iteratively solving the coupled equations.

Since we can include only a limited number of terms in the partial wave expansion it is important to choose which terms to keep according to their relative importance in the overall expansion. It is not possible to know *a priori* the optimal ordering for choosing partial waves but, for the most part, partial wave terms should be added to the expansion in the order of increasing (l_1, l_2) . Applying this simplistic ‘‘rule-of-thumb’’ is more complicated for large L where $|l_1 - l_2|$ can be large. The partial wave terms included in our calculations are listed in Table I. Note that only terms with $l_1\leq l_2$ are listed since all terms with $l_2>l_1$ are included when solving the coupled equations. This particular choice of partial waves is better suited for singlet rather than triplet calculations because the antisymmetry requirements of the triplet wave function require that partial waves with $l_1=l_2$ will have much less importance.

In order to ensure convergence of our truncated partial wave expansion we initially solved the coupled equations for each value of L with fewer terms than what is listed in Table I. We then incrementally increased the number of partial waves included until doing so no longer had noticeable effects on the partial waves originally included. The lists in Table I indicate the number of terms needed to converge the partial wave expansions for the first ten values of L in our calculations.

A representative radial function for each of the three symmetry classes (symmetric, antisymmetric, and asymmetric) is shown in Fig. 4. All three examples are for 17.6-eV incident energy. Each radial function was computed on a grid that is real out to $130a_0$. These pictures provide a striking visualization of the very different characteristics of the discrete channel and the ionization components of the scattered wave.

The discrete channels all describe states with one electron

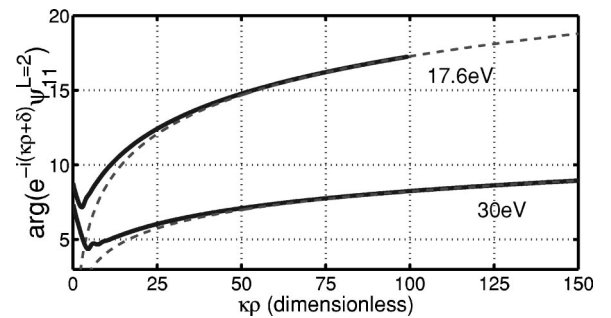


FIG. 6. Development of the logarithmic term in the phase of $\psi_{l_1 l_2}^L$. Results are shown at 17.6 and 30 eV for $L=2$ and $l_1=l_2=1$, along $r_1=r_2$, along with a best fit (dashed lines), using the asymptotic form $(A/\sqrt{\rho})e^{i[\kappa\rho+B\ln(\kappa\rho)+\delta]}$ where A , B and δ are real numbers.

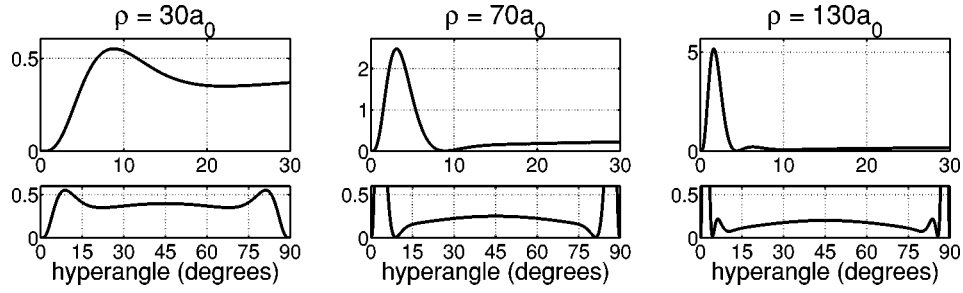


FIG. 7. Flux, as a function of the hyperangle, calculated for various values of the hyperradius ρ for the $L=0, l_1=l_2=1$ radial function with an incident energy of 17.6 eV. The flux is symmetric about 45° . The upper figures detail the discrete channel contributions that dominate the small α regions while the lower figures show the smaller ionization component.

remaining bound to the nucleus. Therefore, these channels are characterized by outgoing waves localized along either the r_1 or the r_2 axis. Exactly which discrete channels are present in a particular radial function is governed by the quantum numbers l_1 and l_2 . For instance, if $l_1=0$ then the radial function along the r_2 axis is dominated by elastic scattering with components for excitation to higher s states also present. When $l_1=1$ then the dominate component along the r_2 axis is the excitation of the $2p$ state.

The ionization continuum, describing both electrons moving away from the nucleus, is characterized by the outgoing circular waves that span the region between the r_1 and r_2 axes. An important characteristic of each radial function is that as the wave fronts propagate away from the origin the discrete channel components remain confined to a certain distance from each edge. That means that if we examine the radial functions along arcs of increasing hyperradius the range of the hyperangle occupied by the discrete channel components decreases and the amount of the ionization component that is “uncovered” increases. This spatial separation of the ionization component from the discrete channels is vital to our method for extracting ionization information from the scattered wave.

Examination of the plots of the radial functions in Fig. 4 reveals that the scattered wave calculated with exterior complex scaling does indeed contain a component with both electrons in the continuum. However, there is still a question

of whether or not this component correctly describes the breakup in a system of three charged particles, particularly given that our formalism requires truncating the Coulomb potentials in the inhomogeneous term $(\hat{H}-E)\Psi_{k_i}^0$ of Eq. (3). The ultimate test of the accuracy of our calculated wave function will be its ability to yield correct differential cross sections for ionization. Before discussing the details of our method for extracting ionization cross sections, which is the subject of the following section, we can give a preliminary indication of the correctness, over a finite region, of our calculated wave function by showing that its asymptotic behavior is consistent with the Rudge asymptotic form in Eq. (6).

We expect the ionization component of each $\psi_{l_1 l_2}^L$ to have the functional form

$$\psi_{l_1 l_2}^L(r_1, r_2) \sim \frac{A(\alpha)}{\sqrt{\rho}} e^{i[\lambda\rho + B(\alpha)\ln(\kappa\rho) + \delta(\alpha)]} \quad (17)$$

of an outgoing circular wave with a logarithmic phase. Since Eq. (6) is valid only when all three particles are widely separated, the radial functions will follow Eq. (17) best along the line $r_1=r_2$. Comparisons between a calculated radial function and the functional form in Eq. (17) both with and without a logarithmic phase term are shown in Fig. 5. In both cases the parameters were chosen to best fit the radial func-

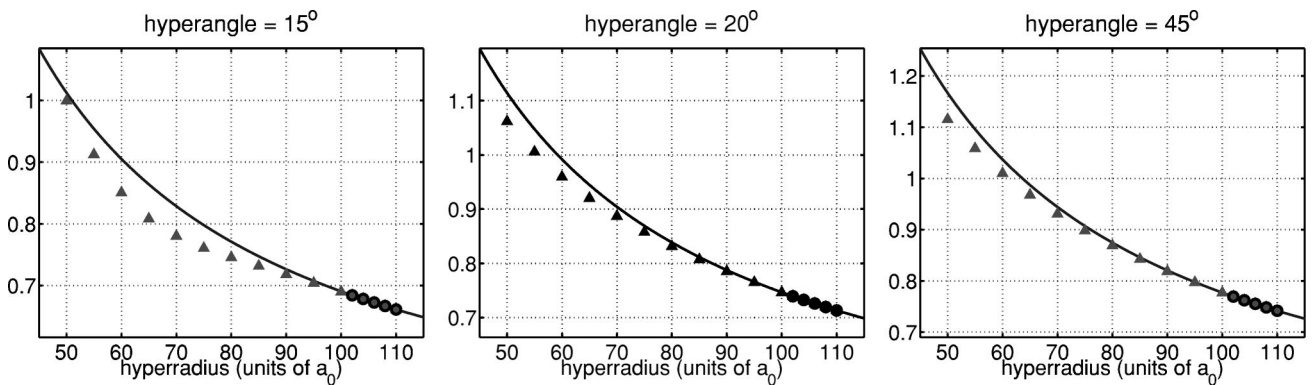


FIG. 8. Comparison of calculated flux to a $1/\rho$ extrapolation curve from the $L=2, l_1=l_2=1$ singlet radial function for 25-eV incident energy. The comparison is done for three different values of the hyperangle. The solid line is the $1/\rho$ least-squares fit and the markers are the values of the flux from the wave function. The values of the flux that were used to produce the least-squares fit are circled.

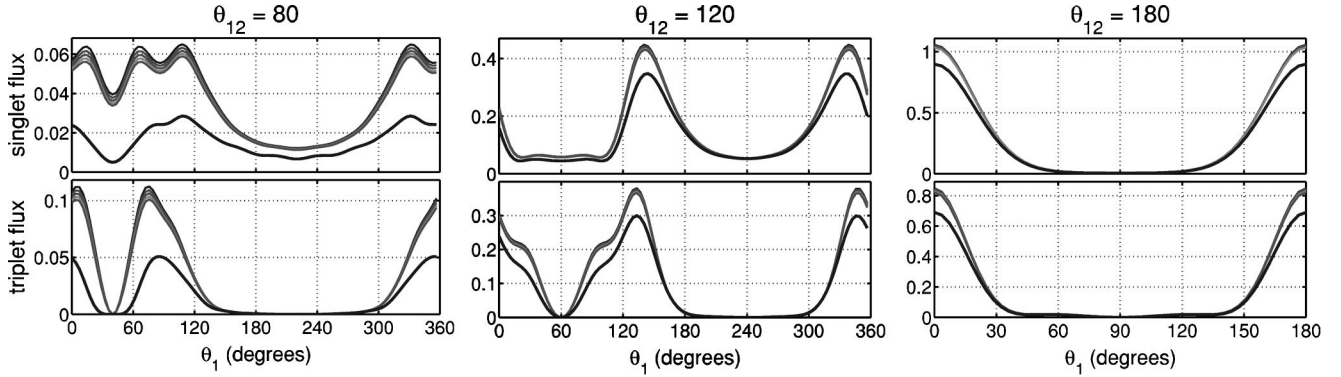


FIG. 9. Extrapolation in ρ of ionization flux for coplanar geometries with fixed θ_{12} at 20-eV incident energy. In each panel flux calculated at $\rho=100, 105, 110, 115,$ and $120a_0$ are shown along with the extrapolated flux. The line for the extrapolated flux always lies below the others.

tion near $r_1=r_2=150a_0$. Without the logarithmic phase term (i.e., setting $B=0$) the functional form is able to match the radial function only over a very small distance. However, with the inclusion of a logarithmic phase term we can fit the phase of the radial function quite well over a very large range. Figure 6 shows how quickly the logarithmic term in the phase develops as the hyperradius increases for two different incident energies. The presence of a logarithmic phase term in the ionization component of the scattered wave suggests that truncating the Coulomb potentials has not seriously damaged the wave function in the interior region. Inspection of Fig. 5 also shows that the amplitude of the ionization component of the scattered wave is not constant, but rather falls as ρ increases. Indeed, a $\rho^{-1/2}$ dependence in the amplitude, along with a logarithmic phase term, are the two key characteristics of Eq. (17). In the following section, we will show how the heuristic observations made here can be developed into a numerical procedure for calculating physical ionization cross sections.

V. EXTRACTING DETAILED INFORMATION ABOUT IONIZATION

A. Flux operator formalism

A complete theoretical treatment of electron-impact ionization must include a prescription for calculating differential cross sections that give detailed information about the energies and angles of ejection of both electrons. Our approach is to obtain such information directly from the radial components of the scattered wave by computing the outgoing flux through the surface of a hypersphere that lies within the volume of coordinate space where both coordinates are real. This is a straightforward extension of the procedure we first applied to the Temkin-Poet model problem [14,16].

Assume, for the moment, that we can isolate Ψ_{ion}^+ , the component of Ψ_{sc}^+ [Eq. (5)] describing the ionization continuum. Equation (6) describes Ψ_{ion}^+ as an outgoing wave in the hyperradius ρ . The continuum of ionization final states is then described by flux through a hypersphere of radius ρ_0 in

the limit $\rho_0 \rightarrow \infty$. To this end, we define a generalized, dimensionless flux $\mathbf{f}_{\rho_0}^{(\text{ion})}$

$$\mathbf{f}_{\rho_0}^{(\text{ion})}(\alpha, \hat{r}_1, \hat{r}_2) \equiv \text{Im} \left[k_i \rho (r_1 r_2 \Psi_{\text{ion}}^+(\mathbf{r}_1, \mathbf{r}_2))^* \times \frac{d}{d\rho} (r_1 r_2 \Psi_{\text{ion}}^+(\mathbf{r}_1, \mathbf{r}_2)) \right]_{\rho=\rho_0} \quad (18)$$

evaluated at a hyperradius ρ_0 . Since the hyperspherical angle α parametrizes the momentum distribution between the two electrons as $\rho_0 \rightarrow \infty$, we can express the total ionization cross section as an integral of $\mathbf{f}_{\rho_0}^{(\text{ion})}$, in the limit $\rho_0 \rightarrow \infty$, over α and the angular coordinates of both electrons,

$$\sigma_{\text{ion}} = \frac{1}{k_i^2} \int_0^{\pi/2} \int_{4\pi} \int_{4\pi} \mathbf{f}_{\rho_0}^{(\text{ion})}(\alpha, \hat{r}_1, \hat{r}_2) d\hat{r}_1 d\hat{r}_2 d\alpha \Big|_{\rho_0 \rightarrow \infty}. \quad (19)$$

Thus, the $\rho_0 \rightarrow \infty$ limit of the flux leads directly to a differential cross section for ionization. However, since we can calculate the wave function only over a finite region we need a means of obtaining the $\rho_0 \rightarrow \infty$ limit from flux calculated at finite ρ_0 .

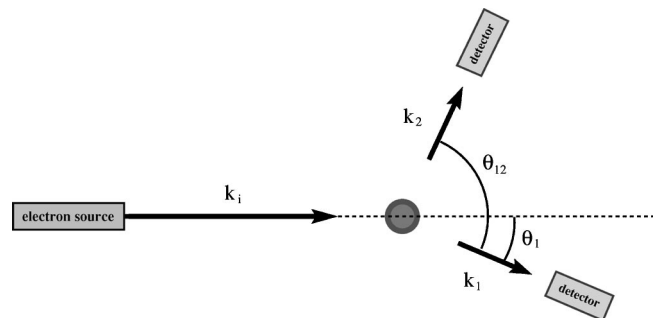


FIG. 10. Diagram of coplanar geometry. Two electron detectors and the incident electron beam all lie within a plane.

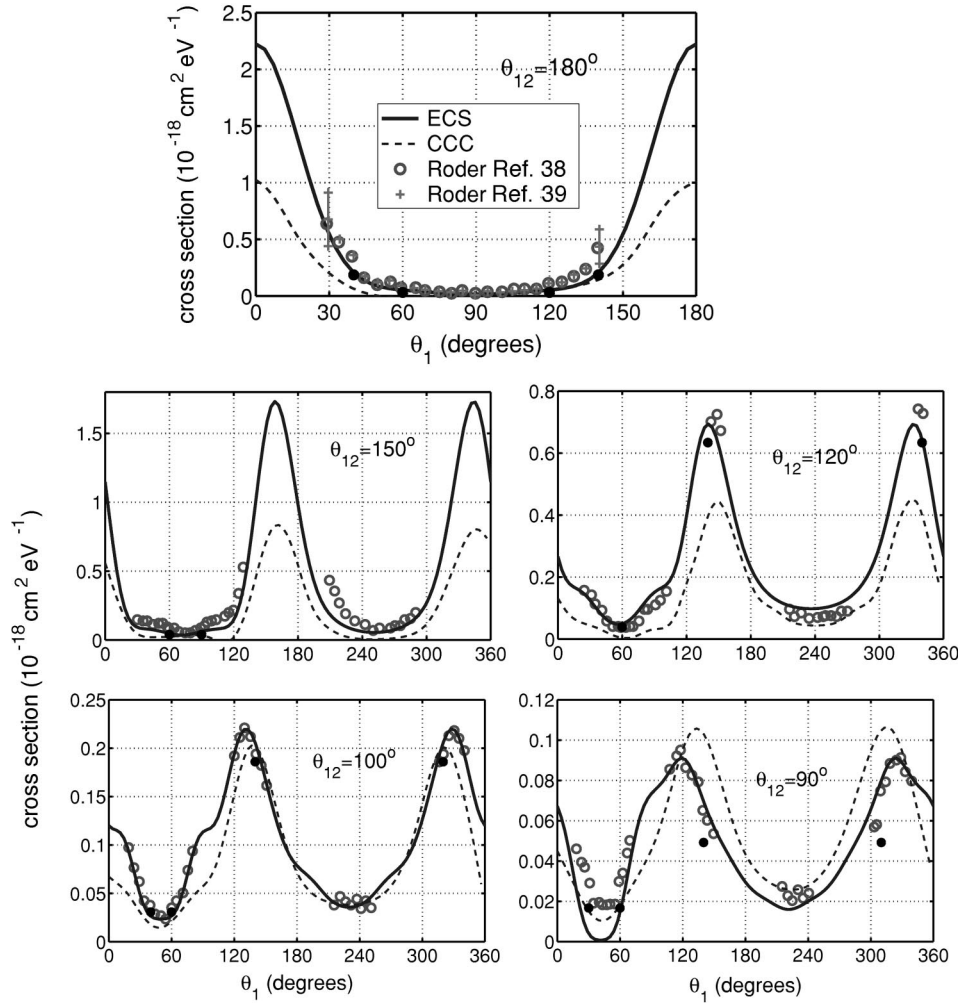


FIG. 11. Equal-energy sharing, coplanar TDCS for 17.6-eV incident energy with θ_{12} fixed. Data from Ref. [38] normalized by comparison with data from Ref. [39] for $\theta_{12}=180^\circ$. Solid curves: present results. Broken curves: CCC results from Ref. [11]. The internormalized data (from Ref. [38]) for different θ_{12} values (open circles) are all set on an absolute scale with a single normalization factor of 0.23, which is chosen on the basis of the data in Ref. [39] for $\theta_{12}=180^\circ$. The full circles are taken from the fixed θ_2 data (see Fig. 12) to check the consistency of our normalization of the latter.

By inserting the asymptotic form for Ψ_{ion}^+ from Eq. (6) into Eq. (18) we find that the ionization flux approaches its asymptotic limit as $1/\rho$, i.e., for large ρ_0

$$\mathbf{f}_p^{(\text{ion})}(\alpha, \hat{r}_1, \hat{r}_2) = \mathbf{f}_z^{(\text{ion})}(\alpha, \hat{r}_1, \hat{r}_2) + O\left(\frac{1}{\rho_0}\right). \quad (20)$$

We can, therefore, obtain the $\rho_0 \rightarrow \infty$ limit of the ionization flux by fitting Eq. (20) to values of $\mathbf{f}_{\rho_0}^{(\text{ion})}$ calculated at large, but finite, ρ_0 . This method requires that the $\mathbf{f}_{\rho_0}^{(\text{ion})}$ must be calculated at ρ_0 large enough so that it is behaving according to Eq. (20), which is easy to test numerically. In addition to ionization channels, the scattered wave also contains components that correspond to discrete (elastic and excitation) two-body processes which leave one electron in a bound Rydberg state. There is interference between these discrete channels and the ionization wave at any finite value of ρ_0 . Thus the notion of a well-defined ionization wave only makes sense in the limit $\rho_0 \rightarrow \infty$ where there is no spatial overlap between discrete channel components and Ψ_{ion}^+ . The practical consequence of this fact is that there are always regions near the r_1 and r_2 axis, i.e., near $\alpha=0$ and $\alpha=90^\circ$, where the calculated flux will not behave according to Eq. (20) due to contamination from discrete channels. The angular range in α

subtended by the flux due to a discrete channel is $\sin^{-1}(\Delta/\rho_0)$, where Δ is the distance over which the target state is appreciably different from zero. Thus as ρ_0 increases, contamination of the ionization flux from discrete channels is confined to smaller regions of α , as illustrated in Fig. 7. With the largest grids we employed, we could directly calculate the ionization flux for values of α down to $\sim 8^\circ$ and then use linear extrapolation to $\alpha=0$. In the true $\rho_0 \rightarrow \infty$ limit the discrete channels' contributions to the flux become δ functions at $\alpha=0$ and $\alpha=90^\circ$ and equality in Eq. (20) holds except for infinitesimally small regions near the edges. We can only calculate the flux where both radial coordinates are real. For α near 45° the f_{ρ_0} can be evaluated for ρ_0 values as large as $\sqrt{2}R_0$ (see Fig. 1), while for small values of α we are limited to $\rho_0 \leq R_0$. Figure 8 shows the behavior of the calculated flux for a single partial-wave component of the scattered wave as a function of ρ_0 for several values of α . Typically, we choose five values of ρ_0 near the end of the real portion of the grid at which to calculate \mathbf{f}_{ρ_0} and obtain the $\rho_0 \rightarrow \infty$ limit by a least-squares fit of Eq. (20). The quality of the extrapolation is, of course, best for α values near 45° since these regions are the first to show the ‘‘uncovering’’ of the ionization wave by the discrete channel components as ρ increases.

B. Calculation of the ionization flux

Calculating the scattered flux requires the assembly of Ψ_{sc}^+ from all of its partial waves. Both Ψ_{sc}^+ and $(d/d\rho)\Psi_{\text{sc}}^+$ in Eq. (18) involve sums over L and (l_1, l_2) pairs so the flux definition in terms of partial waves

$$\mathbf{f}_{\rho_0}(\alpha, \hat{r}_1, \hat{r}_2) = \text{Im} \left\{ k_i \rho \sum_{\substack{L', l'_1, l'_2 \\ L, l_1, l_2}} (\psi_{l'_1 l'_2}^{L'})^* \frac{d}{d\rho} (\psi_{l_1 l_2}^L) \right. \\ \left. \times (\mathcal{Y}_{l'_1 l'_2}^{L'})^* \mathcal{Y}_{l_1 l_2}^L \right\} \Bigg|_{\rho=\rho_0} \quad (21)$$

involves cross terms between different partial waves. Because of these cross terms, the flux must first be ‘‘assembled’’ according to Eq. (21) and then extrapolated when we are calculating angular distributions. Three examples of calculated and extrapolated flux, for both singlet and triplet spin symmetries with $\alpha=45^\circ$, are shown in Fig. 9. These examples are for coplanar geometries with a fixed angle θ_{12} between the outgoing electrons (see Fig. 10). Relative differences between the calculated and extrapolated flux are largest when the angle between the outgoing electrons is smallest. When constructing \mathbf{f}_{ρ_0} as in Eq. (21) it is important to remember to include both $\psi_{l_1 l_2}^L$ and $\psi_{l_2 l_1}^L$ when $l_1 \neq l_2$.

The number of partial waves required to converge the flux depends not only on the total energy but also on the directions of the two outgoing electrons. In the present calculations, we kept partial waves through $L=9$, which was sufficient for the geometries considered here. Convergence in L is most rapid when the angle between the ejected electrons is 180° and becomes increasingly slower as this angle is decreased. The number of (l_1, l_2) pairs for each L that were kept in the calculations was determined when solving the coupled equations, as discussed in the preceding section.

Ionization cross sections can be readily expressed in terms of the scattered flux. The triply differential cross section (TDCS) is defined as the quantity that gives the total ionization cross section when integrated over the directions of both electrons and the energy ε of one of the outgoing electrons

$$\sigma_{\text{ion}} = \int_0^{E/2} \int_{4\pi} \int_{4\pi} \frac{d\sigma_{\text{ion}}(\varepsilon, \hat{r}_1, \hat{r}_2)}{d\varepsilon d\hat{r}_1 d\hat{r}_2} d\hat{r}_1 d\hat{r}_2 d\varepsilon. \quad (22)$$

Since the electrons are indistinguishable, it is customary to normalize the TDCS so that it gives σ_{ion} when integrated over half the energy range. The individual electron energies are parametrized by the hyperangle α [22]

$$\varepsilon_1 = E \cos^2 \alpha \quad \text{and} \quad \varepsilon_2 = E \sin^2 \alpha \quad (23)$$

and thus a simple change of variables converts the flux, which is differential in α , to the TDCS, which is differential in ε ,

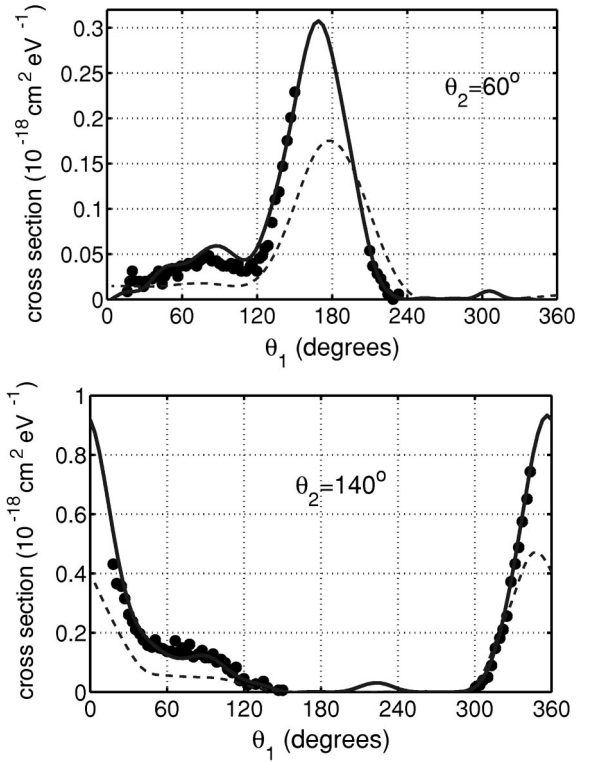


FIG. 12. Equal-energy sharing, coplanar TDCS for 17.6-eV incident energy with θ_2 fixed. Internormalized measurements from Ref. [38], reported in arbitrary units, were scaled by 1.15 to the best-fit calculated cross section. Solid curves: present results. Broken curves: CCC results from Ref. [11].

$$\frac{d\sigma_{\text{ion}}(\varepsilon, \hat{r}_1, \hat{r}_2)}{d\varepsilon d\hat{r}_1 d\hat{r}_2} \Bigg|_{\varepsilon=E \sin^2 \alpha} \\ = \lim_{\rho_0 \rightarrow \infty} \frac{1}{k_i^2 E \sin \alpha \cos \alpha} \mathbf{f}_{\rho_0}(\alpha, \hat{r}_1, \hat{r}_2). \quad (24)$$

The ionization flux cannot be extrapolated for hyperangles near $\alpha=0$ and $\alpha=90^\circ$ so this procedure cannot produce the TDCS for highly asymmetric energy sharing, i.e., for cases where one electron carries most of the total energy.

The singly differential cross section (SDCS) describes only energy sharing between the two electrons and is obtained by integrating the TDCS over the directions of both electrons:

$$\frac{d\sigma_{\text{ion}}(\varepsilon)}{d\varepsilon} = \int_{4\pi} \int_{4\pi} \frac{d\sigma_{\text{ion}}(\varepsilon, \hat{r}_1, \hat{r}_2)}{d\varepsilon d\hat{r}_1 d\hat{r}_2} d\hat{r}_1 d\hat{r}_2. \quad (25)$$

Orthonormality of the $\mathcal{Y}_{l_1 l_2}^{LM}$ simplifies the summation in Eq. (21) to a single sum over the three angular momentum quantum numbers. The SDCS is then a simple sum of contributions from each partial wave:

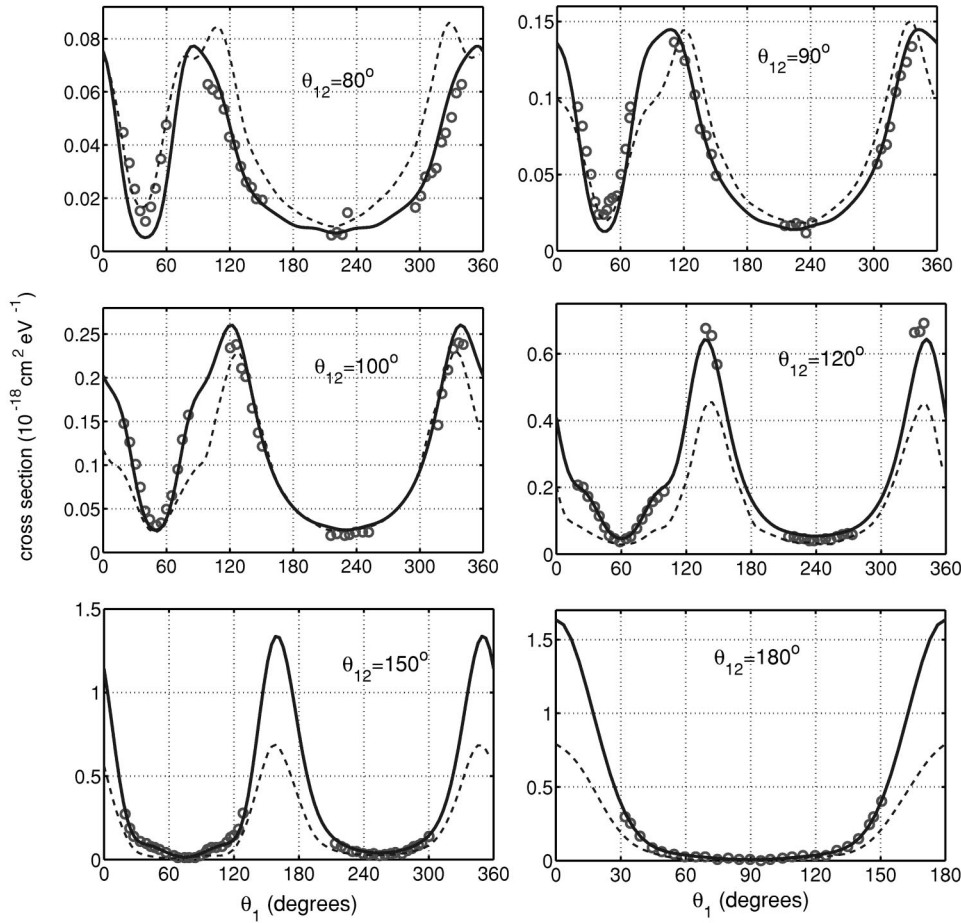


FIG. 13. Equal-energy sharing, coplanar TDCS for 20-eV incident energy with θ_{12} fixed. Internormalized measurements from Ref. [38], reported in arbitrary units, were scaled by 0.20 to the best-fit calculated cross section. Solid curves: present results. Broken curves: CCC results from Ref. [11].

$$\left. \frac{d\sigma_{\text{ion}}(\varepsilon)}{d\varepsilon} \right|_{\varepsilon=E \sin^2 \alpha} = \frac{\rho}{k_i E \sin \alpha \cos \alpha} \times \sum_{L, l_1, l_2} \text{Im} \left\{ [\psi_{l_1 l_2}^L(r_1, r_2)]^* \frac{d}{d\rho} \times [\psi_{l_1 l_2}^L(r_1, r_2)] \right\} \Bigg|_{\rho \rightarrow \infty}. \quad (26)$$

Since there are no cross terms in the SDCS expression, we can sum the individually extrapolated ($\rho_0 \rightarrow \infty$) partial-wave flux components. In general, significantly fewer partial-wave terms are needed to converge the SDCS than are needed to converge the TDCS. For the incident energies we report here there was no need to include contributions for $L > 6$. The SDCS is symmetric about $E/2$, in accordance with the ‘‘symmetrization postulate’’ of the formal theory [37]. This property follows naturally from our treatment since the cross sections are extracted directly from radial wave functions which themselves display the proper symmetry with respect to interchange of electrons.

Other quantities of interest that we report are the total cross section,

$$\sigma_{\text{ion}} = \frac{1}{4} (\sigma_S + 3\sigma_T), \quad (27)$$

and the spin asymmetry which is identically equal to

$$\frac{\sigma_S - \sigma_T}{\sigma_S + 3\sigma_T}, \quad (28)$$

where the singlet and triplet total cross sections, σ_S and σ_T (defined here without inclusion of spin statistical weights), are obtained by integrating the corresponding SDCS values over ε .

VI. DIFFERENTIAL CROSS SECTIONS FOR IONIZATION

The availability of *absolute* experimental values of the TDCS at low impact energies offers the most stringent test for judging the fundamental correctness of any method that proposes to correctly treat the three-body Coulomb problem from first principles. There are many examples of approximate methods that give excellent results only for specific exit geometries and energy asymmetries [7] or that give very good relative differential cross sections, yet fail to predict the correct magnitudes of those quantities [10,11]. Absolute experimental data are fortunately available for the case of equal energy sharing ($\varepsilon_1 = \varepsilon_2 = E/2$) at a specific set of coplanar geometries. Most experimental data have been taken for geometries where the two detectors are rotated together while keeping the angular separation θ_{12} between them (see Fig. 10) fixed.

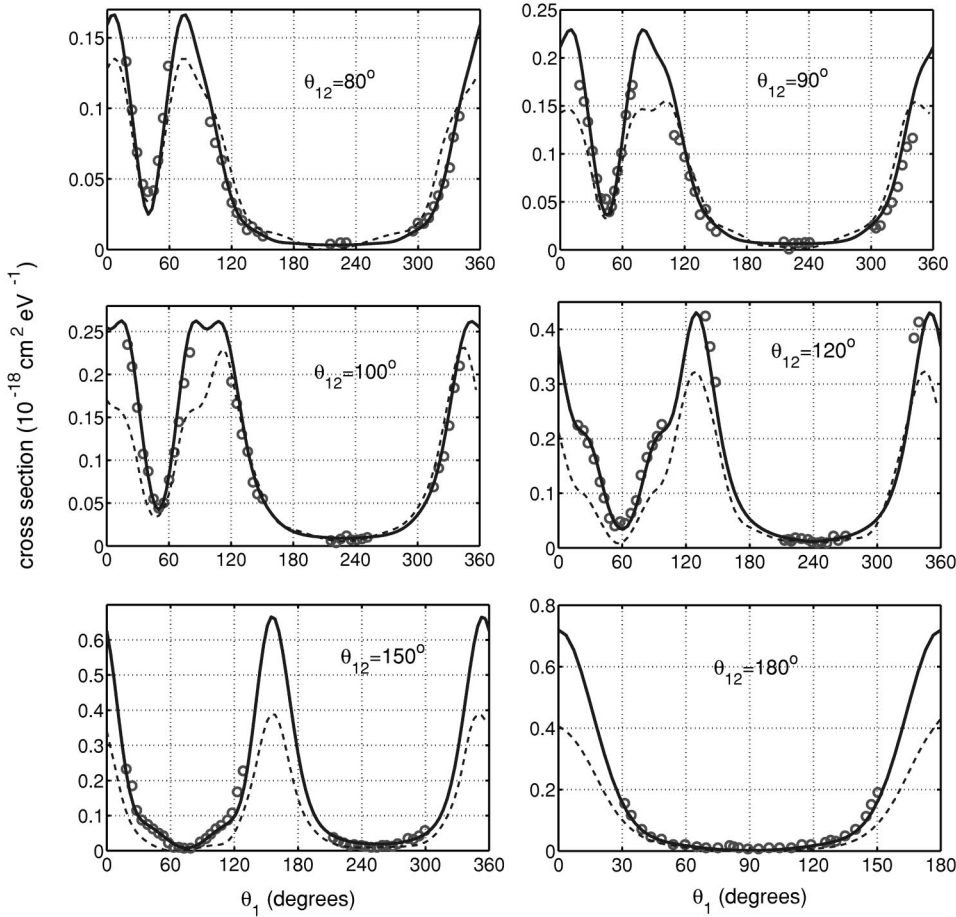


FIG. 14. As in Fig. 13 for 25-eV incident energy. Scale factor used to normalize experimental data is 0.16.

In 1996, Röder *et al.* [38] published a set of TDCS data for e -H ionization for coplanar geometries. These data were not absolute, but were “internormalized.” For each energy, a single, geometry-independent scaling factor is needed to normalize the data, but that factor depends on energy. Röder *et al.* [39] later presented a small set of absolute measurements in Ref. [39] at 15.6- and 17.6-eV incident energy, for the case where θ_{12} was fixed at 180° . We have used the data from Ref. [39] at 17.6 eV to put their earlier data on an absolute scale. These TDCS values are shown in Fig. 11 along with our calculated values. The top panel shows both the absolute data from Ref. [39] and the normalized data from Ref. [38], which are mutually consistent and in good agreement with our calculated values. The cross section in this case is strongly peaked at angles of 0° and 180° , where one electron is scattered forward and the other recoils in the backward direction. The next four panels in Fig. 11 with fixed θ_{12} values compare the normalized values from Ref. [38] with our calculations. Overall, there is excellent agreement. The largest discrepancy is at the minimum for $\theta_{12} = 90^\circ$. The cross-section set is smallest for this geometry and converging the TDCS in partial waves becomes increasingly difficult as θ_{12} decreases.

Figure 12 also shows 17.6-eV data from the measurements of Ref. [38], but for these cases one detector was held fixed and the other was rotated independently. These data have a normalization which is different from the fixed θ_{12}

data, so for these two panels, we chose a single scale factor that gives the best fit to our calculated cross section. As a consistency check, we extracted those data points from the fixed θ_{12} measurements that had corresponding points in the fixed θ_{12} data and plotted them along with the latter in Fig. 11. Where comparison is possible, the agreement is good.

We have also plotted in Figs. 11 and 12 the recent convergent close-coupling (CCC) results of Bray [11] for comparison. The agreement between our calculations and CCC is somewhat mixed and decidedly geometry dependent. For the three largest θ_{12} data sets shown in Fig. 11, the CCC results are roughly a factor of two smaller than our results, but agree reasonably well in shape. At the two other angles, the magnitude of the CCC cross sections near the peaks is roughly the same as our results, but there are noticeable differences in the shapes, with the CCC showing narrower peaks that are slightly shifted relative to experiment with more significant discrepancies near the troughs. For the fixed θ_{12} data in Fig. 12, there are also noticeable differences, with CCC showing peak values that are roughly half of what we find and slightly shifted relative to experiment. Röder *et al.* [39] have also presented distorted partial wave results of Pan and Starace [5], which is only available for $\theta_{12} = 180^\circ$. These results (not shown) are in good agreement with our calculations.

Comparison between the calculated equal-energy sharing coplanar TDCS with fixed θ_{12} and values measured by Röder *et al.* [38] for 20-, 25-, and 30-eV incident energies are

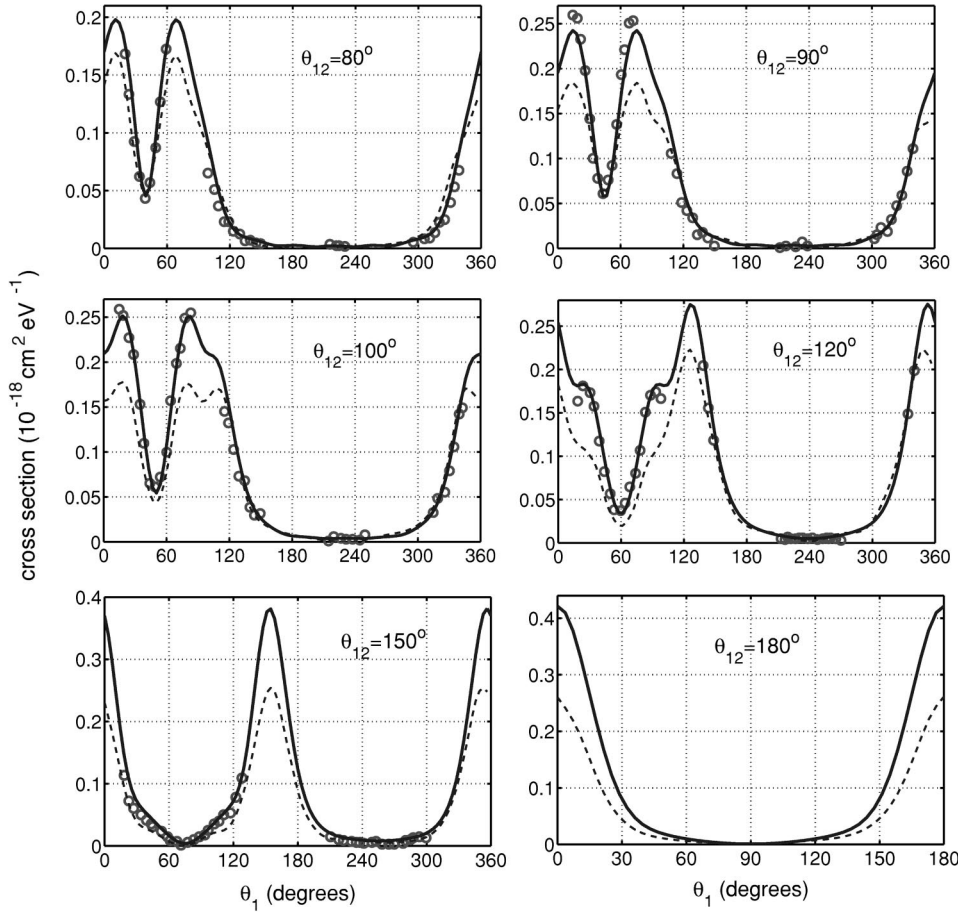


FIG. 15. As in Fig. 13 for 30-eV incident energy. Scale factor used to normalize experimental data is 0.16.

shown in Figs. 13–15. At these energies, the experimental values are unfortunately known only in the originally reported arbitrary units. We chose a single scaling factor for each energy that normalizes the experimental values to known units. Agreement between theory and experiment is excellent over this range of geometries with the largest discrepancies generally occurring for smaller values of θ_{12} where the effects from truncating the partial wave expansion of Ψ_{sc}^+ are most significant. Recent CCC calculations [11] included results for these energies as well and are shown for comparison. The situation is basically the same as with the 17.6-eV data. At the largest θ_{12} values, the CCC results are consistently smaller than ours, while at the smaller θ_{12} values, there is less discrepancy in magnitude, but more pronounced differences in the peak positions and shapes. It is entirely possible that these latter differences may be related to difficulties associated with partial wave convergence which is most difficult at small values of θ_{12} . Overall, there is no single scaling that suffices to bring the CCC results at a particular energy into uniform agreement with our results. Distorted partial wave results (not shown) are also available at these energies, but only for $\theta_{12}=180^\circ$ [39]. Once again, the agreement with our results was found to be quite good.

The SDCS reduces to an incoherent sum of partial wave components according to Eq. (26). For values of α away from 0° and 45° , the individual L components were extrapolated to infinite ρ_0 from calculated values. The inability to

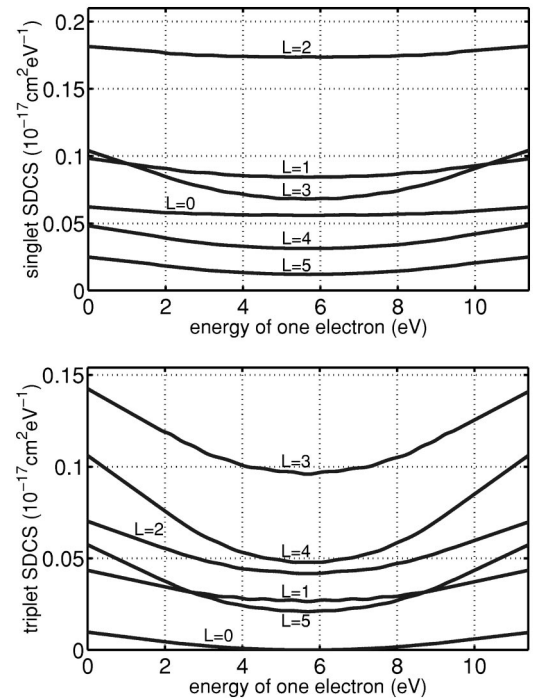


FIG. 16. Components of the SDCS (with spin factors included) for electron-hydrogen scattering at 25-eV incident energy corresponding to particular total spin and angular-momentum quantum numbers.

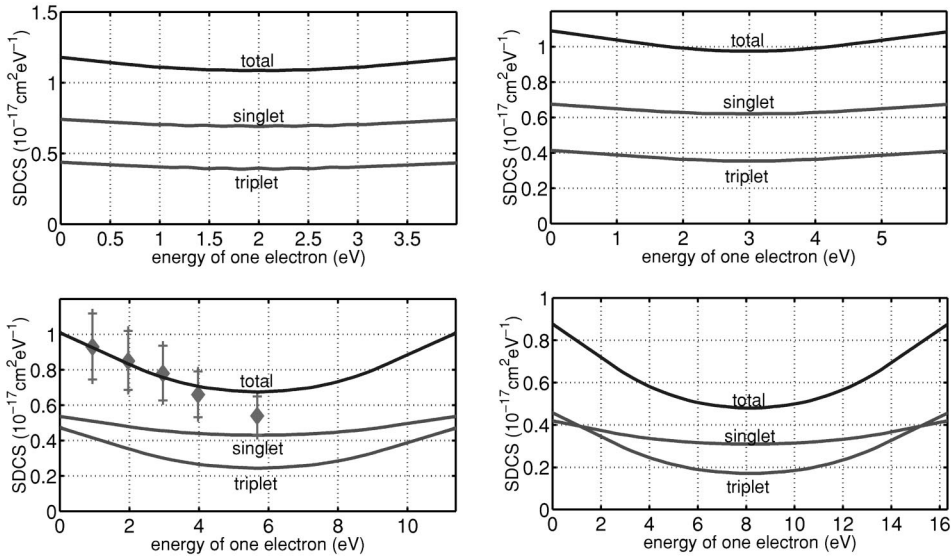


FIG. 17. Single differential cross sections for electron-hydrogen scattering at 17.6-eV (top left), 20-eV (top right), 25-eV (bottom left), and 30-eV (bottom right) incident energies. The cross sections for singlet and triplet spin symmetries (with spin factors included) are shown along with the total. The 25-eV data are compared to the experiment of Shyn [40].

distinguish, at finite distances, between ionization and excitation of high- n Rydberg states prevented us from directly calculating the SDCS within $5\text{--}10^\circ$ of $\alpha=0$ and 90° , depending on the energy and L value considered. To extend the SDCS into these ranges, we used a linear extrapolation of the SDCS as a function of ε to $\varepsilon=0$ and $\varepsilon=E$.

We show individual contributions to the 25 eV incident energy SDCS for different values of L and S in Fig. 16. Each of these components is symmetric about $\varepsilon=E/2$, reflecting the indistinguishability of the electrons. The triplet $L=0$ must vanish at $\varepsilon=E/2$ since it is extracted only from anti-symmetric radial functions and it contributes negligibly to the total SDCS. We found this to be the case at the other energies we studied as well. We found that the SDCS generally converged faster as a function of L than did the TDCS.

Singlet and triplet components, along with the total, of the SDCS for 17.6-, 20-, 25-, and 30-eV incident energy are shown in Fig. 17. There is a marked bowing of the SDCS that occurs as the energy increases, which is evidently attributable to the triplet component, while the singlet contribution shows less dependence on ejected electron energy over the whole range of incident energies considered. For 25-eV incident energy, we have plotted the data reported by Shyn [40]. Our calculated SDCS for this energy is in good agreement with Shyn's data except for the one value at $E/2$ where our calculated value falls outside the reported error bars. Interestingly, this value corresponds to $\alpha=45$, the point at

which there is the least uncertainty associated with our extrapolation. We hasten to point out, however, that Shyn's values were determined by integrating measured values of the doubly differential cross section and the latter had to be extrapolated through small and large angular regions where measurements could not be made.

Finally, we list values of the integrated ionization cross sections and spin asymmetries in Table II. These provide a rather coarse measure of the ionization dynamics and are quantities that are adequately described by other theoretical methods as well.

VII. DISCUSSION

The complexity of the asymptotic form of the wave function for three charged particles and the fact that it is only known in the "far" asymptotic region has been a major bottleneck in the development of practical *ab initio* computational approaches to electron-impact ionization. We have side stepped the problem by using a mathematical transformation of the Schrödinger equation that effectively turns the scattered wave into a bound state. Exterior complex scaling provides us with a method for computing the physically correct wave function over a finite region of space without explicit specification of asymptotic boundary conditions. The accuracy of the computed wave function is limited only by the finite size of the grid and the number of partial waves retained. The errors in the wave function can, in principle, be made arbitrarily small given sufficient computing power.

It is also worth noting that grid-based wave-packet methods, based on solving the time-dependent Schrödinger equation, are also being developed to study electron-impact ionization [41,42]. These approaches also avoid explicit enforcement of asymptotic boundary conditions for breakup, so it will be interesting to see if they will be able to provide the kind of detailed differential cross-section information of the type presented here.

The principle sources of uncertainty in the computed ionization cross sections are related more to the particular meth-

TABLE II. Singlet, triplet, and total ionization cross sections and the spin asymmetry. Cross sections are in units of a_0^2 , asymmetry is dimensionless. Spin factors are not included in the singlet and triplet cross sections.

Incident energy	17.6 eV	20 eV	25 eV	30 eV
Singlet	2.027	2.741	3.807	4.036
Triplet	0.389	0.538	0.885	1.047
Total	0.798	1.089	1.616	1.794
Asymmetry	0.513	0.506	0.452	0.416

TABLE III. Seven-point finite difference formulas for the ‘‘interface’’ between two regions with grid spacings g and h . Special formulas are needed for the second derivative at the interface point x_p as well as two points on either side. The columns of the table give the coefficients needed to approximate f_n^{ii} for $n=p\pm 2$, $n=p\pm 1$, and $n=p$. When $n>p$ the spacings g and h must be permuted.

	$n=p\mp 2$	$n=p\mp 1$	$n=p$
$f_{n\mp 3}$	$\frac{1}{15g(5g+h)}$	$\frac{3g^2+3gh-2h^2}{24g^2(2g+h)(4g+h)}$	$\frac{2(11g-9h)h^2}{9g^2(g+h)(3g+h)(3g+2h)}$
$f_{n\mp 2}$	$\frac{-(8g+h)}{12g^2(4g+h)}$	$\frac{-(5g^2+6gh-2h^2)}{3g^2(3g+h)(3g+2h)}$	$\frac{-3(11g-8h)h^2}{2g^2(g+h)(2g+h)(2g+3h)}$
$f_{n\mp 1}$	$\frac{2(7g+2h)}{3g^2(3g+h)}$	$\frac{13g^2+21gh+2h^2}{4g^2(g+h)(2g+h)}$	$\frac{6(11g-5h)h^2}{g^2(g+h)(g+2h)(g+3h)}$
f_n	$\frac{-(34g+15h)}{6g^2(2g+h)}$	$\frac{-(9g^2+30gh+10h^2)}{3g^2(g+h)(g+2h)}$	$\frac{36g^2-121gh+36h^2}{18g^2h^2}$
$f_{n\pm 1}$	$\frac{5g+4h}{3g^2(g+h)}$	$\frac{22h^2+15hg-g^2}{24g^2h^2}$	$\frac{6g^2(11h-5g)}{h^2(g+h)(2g+h)(3g+h)}$
$f_{n\pm 2}$	$\frac{-(4g+5h)}{60g^2h}$	$\frac{-2g^3(10h-g)}{h^2(g+h)(2g+h)(3g+h)(4g+h)}$	$\frac{-3g^2(11h-8g)}{2h^2(g+h)(g+2h)(3g+2h)}$
$f_{n\pm 3}$	$\frac{8g^4}{h(g+h)(2g+h)(3g+h)(4g+h)(5g+h)}$	$\frac{g^3(5h-g)}{4h^2(g+h)(2g+h)(g+2h)(3g+2h)}$	$\frac{2g^2(11h-9g)}{9h^2(g+h)(g+3h)(2g+3h)}$
Error	$-\frac{1}{630}g^4(g-h)f_n^{vii}$	$-\frac{1}{2520}g^3(7g+10h)(g-h)f_n^{vii}$	$-\frac{11}{420}g^2h^2(g-h)f_n^{vii}$

ods we have used to extract dynamical information than they are to any errors in the underlying wave functions. The flux operator approach we employed requires us to calculate the wave function at large distances, since it relies on an uncovering of the ionization wave by discrete two-body components that only occurs at large distances. This observation puts practical limitations on our ability to compute singly and triply differential cross sections for highly asymmetric energy-sharing cases which sample regions of space where it is impossible to disentangle the discrete and breakup channels. Going to even larger grids will be possible as computers improve, but will never allow arbitrarily small energy for one electron.

There is much evidence to suggest that the techniques used to extract cross sections from a computed wave function can dramatically affect the accuracy of the results in a way that is not necessarily connected to the accuracy of the wave function. For example, we recently showed that we could take an accurate wave function, computed by ECS, and produce an unphysical SDCS by matching it to an expansion in discrete two-body pseudostates [12]. It is by no means clear that the flux approach we have used here is in any sense the only way, or the optimum way, to extract the ionization cross sections. Our recent work [43] on integral expressions for breakup cross sections (with short-range potentials) shows them to be far more economical, and reliable, than a direct evaluation of the flux. More work will be required to see if these techniques can be used in the case of Coulomb interactions. It is also possible that some sort of asymptotic

matching scheme is a viable alternative to the approach we have used here, once an accurate wave function is in hand. These are clearly areas ripe for future investigation.

Note added in proof. We were recently made aware of earlier work by Brauner *et al.* [44] in which *internormalized* TDCS for fixed θ_{12} and fixed θ_2 at 17.6 eV were reported. However, as Bray has recently pointed out [11], there are internal inconsistencies in the 17.6 eV data that cast doubt on this internormalization. In view of these inconsistencies in the experimental data, we feel that our independent normalization of the fixed θ_{12} 17.6 eV data (shown in Fig. 12) is reasonable.

ACKNOWLEDGMENTS

This work was performed under the auspices of the U.S. Department of Energy by the University of California Lawrence Berkeley National Laboratory and Lawrence Livermore National Laboratory under Contract Nos. DE-AC03-76SF00098 and W-7405-Eng-48, respectively. The calculations were performed on the SGI/Cray T3E computer at the National Energy Research Scientific Computing Center and the IBM Blue-Pacific computer at LLNL. M. B. acknowledges support from the U.S. DOE Office of Basic Energy Science, Division of Chemical Sciences.

APPENDIX: FINITE DIFFERENCE FORMULAS

Finite difference formulas approximate f_n^{ii} , the second derivative of $f(x)$ evaluated at the grid point x_n , in terms of

$f(x)$ evaluated at x_n and two or more nearby grid points. The function's values at each nearby grid point are expressed as Taylor-series expansions about $x = x_n$. Finite difference formulas are arrived at by taking appropriate linear combinations of these expansions so that the first derivative and as many higher derivative terms as possible vanish. The number of higher derivative terms that can be made to vanish, and the accuracy of the finite difference approximation, depends upon the number of grid points used in the formulas.

In our calculations we used seven-point, central difference formulas that use $f_{n\pm 3}$, $f_{n\pm 2}$, $f_{n\pm 1}$ [$f(x)$ evaluated at $x = x_{n\pm 3}$, $x_{n\pm 2}$, $x_{n\pm 1}$] and f_n to approximate f_n^{ii} . If the grid is evenly spaced, $x_{n+j} = x_n + jh$, then the seven-point finite difference formula

$$f_n^{ii} \approx \frac{1}{h^2} \left(\frac{1}{90} f_{n-3} - \frac{3}{20} f_{n-2} + \frac{3}{2} f_{n-1} - \frac{49}{18} f_n + \frac{3}{2} f_{n+1} - \frac{3}{20} f_{n+2} + \frac{1}{90} f_{n+3} \right) + \frac{69}{25200} h^6 f_n^{viii} \quad (\text{A1})$$

is accurate to sixth order in the grid spacing h . The last term in Eq. (A1) is the leading error term and is given only to indicate the accuracy of the approximation.

When using complex coordinates the parameter h in the Taylor-series expansions may be complex. For instance, Taylor-series expansions relating function values at two grid points on the complex part of the contour defined in Eq. (14) will be in terms of powers of $h = |h|e^{i\eta}$. Equation (A1) can be used to approximate second derivatives at most points on both the real and complex portions of the grid. However, when the seven-point "stencil" defined by Eq. (A1)

straddles the complex turning point R_0 (or an interface between two regions with different grid spacing) other formulas must be used.

Let x_p be either the complex turning point R_0 or an interface point between two regions with different grid spacing. Special formulas are needed to approximate the second derivative at the point x_p and at the two points on either side of x_p . In general, a seven-point finite difference formula has the form

$$f_n^{ii} \approx \sum_{j=-3}^3 a_j f_{n+j}, \quad (\text{A2})$$

where the coefficients a_j are given by Eq. (A1) if x_n is more than two grid points from an interface point. The coefficients needed for the cases $n=p$, $p \pm 1$, or $p \pm 2$ are listed in Table III. Let g and h be the "grid spacings" (possibly complex) on the left and right side of x_p so that $x_{p-j} = x_p - jg$ and $x_{p+j} = x_p + jh$, where j is positive. The coefficients a_j needed in Eq. (A2) to approximate f_n^{ii} when $n=p-2$, $p-1$ or p are found by reading down the appropriate column in Table III. For $n=p+1$ or $p+2$ the coefficients a_j are found by reading up the appropriate column and permuting g and h .

The leading error terms are listed at the bottom of Table III. These seven-point formulas are accurate to fifth order in the grid spacing. In general, finite difference formulas that straddle two regions of different grid spacings will be less accurate by one order than their uniform grid counterparts. For this reason high-order finite difference formulas, such as those presented here, are essential when different grid spacings and/or exterior complex scaling are used.

-
- [1] R. K. Peterkop, *Opt. Spectrosc.* **13**, 87 (1962).
[2] M. R. H. Rudge and M. J. Seaton, *Proc. R. Soc., London, Ser. A* **283**, 262 (1965).
[3] E. O. Alt and A. M. Mukhamedzhanov, *Phys. Rev. A* **47**, 2004 (1993).
[4] M. Brauner, J. S. Briggs, and H. Klar, *J. Phys. B* **22**, 2265 (1989).
[5] C. Pan and A. F. Starace, *Phys. Rev. Lett.* **67**, 185 (1991).
[6] S. Jones, D. H. Madison, and D. A. Kononov, *Phys. Rev. A* **55**, 444 (1997).
[7] S. P. Lucey, J. Rasch, and C. T. Whelan, *Proc. R. Soc. London, Ser. A* **455**, 349 (1999).
[8] I. Bray and A. T. Stelbovics, *Phys. Rev. Lett.* **70**, 746 (1993).
[9] I. Bray, *Phys. Rev. Lett.* **78**, 4721 (1997).
[10] I. Bray and D. Fursa, *Phys. Rev. A* **54**, 2991 (1996).
[11] I. Bray, *J. Phys. B* **33**, 581 (2000).
[12] T. N. Rescigno, C. W. McCurdy, W. A. Isaacs, and M. Baertschy, *Phys. Rev. A* **60**, 3740 (1999).
[13] C. W. McCurdy, T. N. Rescigno, and D. A. Byrum, *Phys. Rev. A* **56**, 1958 (1997).
[14] C. W. McCurdy and T. N. Rescigno, *Phys. Rev. A* **56**, R4369 (1997).
[15] B. Simon, *Phys. Lett.* **71A**, 211 (1979).
[16] M. Baertschy, T. N. Rescigno, W. A. Isaacs, and C. W. McCurdy, *Phys. Rev. A* **60**, R13 (1999).
[17] A. Temkin, *Phys. Rev.* **126**, 130 (1962).
[18] R. Poet, *J. Phys. B* **11**, 3081 (1978).
[19] T. N. Rescigno, M. Baertschy, W. A. Isaacs, and C. W. McCurdy, *Science* **286**, 2474 (1999).
[20] T. N. Rescigno, M. Baertschy, D. Byrum, and C. W. McCurdy, *Phys. Rev. A* **55**, 4253 (1997).
[21] S. Jones and A. T. Stelbovics, *Phys. Rev. Lett.* **84**, 1878 (2000).
[22] M. R. H. Rudge, *Rev. Mod. Phys.* **40**, 564 (1968).
[23] I. C. Percival and M. J. Seaton, *Proc. Cambridge Philos. Soc.* **53**, 654 (1957).
[24] W. P. Reinhardt, *Annu. Rev. Phys. Chem.* **33**, 223 (1982).
[25] C. W. McCurdy and T. N. Rescigno, *Phys. Rev. Lett.* **41**, 1364 (1978).
[26] S. Yabushita, C. W. McCurdy, and T. N. Rescigno, *Phys. Rev. A* **36**, 3146 (1987).
[27] M. Pont and R. Shakeshaft, *Phys. Rev. A* **51**, 494 (1995).
[28] J. Nuttall and H. L. Cohen, *Phys. Rev.* **188**, 1542 (1969).
[29] P. B. Kurasov, A. Scrinzi, and N. Elander, *Phys. Rev. A* **49**, 5095 (1994).
[30] R. Barrett, M. Berry, T. Chan, J. Demmel, J. Donato, J. Don-

- garra, V. Eijkhout, V. Pozo, C. Romine, and H. van der Vorst, *Templates for the Solution of Linear Systems: Building Blocks for the Iterative Methods* (SIAM, Philadelphia, 1994).
- [31] E. Anderson, Z. Bai, C. Bischof, S. Blackford, J. Demmel, J. Dongarra, J. D. Croz, A. Greenbaum, S. Hammarling, A. McKenney, and D. Sorensen, *LAPACK Users' Guide, Release 3.0* (SIAM, Philadelphia, 1999).
- [32] J. George, SIAM (Soc. Ind. Appl. Math.) J. Numer. Anal. **10**, 345 (1973).
- [33] J. W. Liu, ACM Trans. Math. Softw. **11**, 141 (1985).
- [34] J. W. Demmel, S. C. Eisenstat, J. R. Gilbert, X. S. Li, and J. W. H. Liu, SIAM J. Matrix Anal. Appl. **20**, 720 (1999).
- [35] J. W. Demmel, J. R. Gilbert, and X. S. Li, Lawrence Berkeley National Laboratory Technical Report No. LBNL-44289, 1999; software is available at <http://www.nersc.gov/~xiaoye/SuperLU>.
- [36] X. S. Li and J. W. Demmel, in *Proceedings of the ACM/IEEE, SC 98 Conference* (IEEE, Los Alamitos, CA, 1998).
- [37] R. K. Peterkop, Proc. Phys. Soc. London **77**, 1220 (1961).
- [38] J. Röder, J. Rasch, K. Jung, C. T. Whelan, H. Ehrhardt, R. Allan, and H. Walters, Phys. Rev. A **53**, 225 (1996).
- [39] J. Röder, H. Ehrhardt, C. Pan, A. F. Starace, I. Bray, and D. Fursa, Phys. Rev. Lett. **79**, 1666 (1997).
- [40] T. W. Shyn, Phys. Rev. A **45**, 2951 (1992).
- [41] M. S. Pindzola and F. J. Robicheaux, Phys. Rev. A **54**, 2142 (1996).
- [42] M. S. Pindzola and F. J. Robicheaux, Phys. Rev. A **61**, 052707 (2000).
- [43] C. W. McCurdy and T. N. Rescigno, Phys. Rev. A (to be published).
- [44] M. Brauner, J. S. Briggs, H. Klar, J. T. Broad, T. Rosel, K. Jung, and H. Ehrhardt, J. Phys. B **24**, 657 (1991).